Journal of Geochemical Exploration 280 (2026) 107889

Contents lists available at ScienceDirect

Journal of Geochemical Exploration

journal homepage: www.elsevier.com/locate/gexplo

Geochemistry and economic evaluation of REE + Y potential in the fine-grained matrix of sedimentary phosphorites from the Tebessa region, eastern Algeria

Riadh Aouachria [a], Rabah Kechiched [a,*], Roberto Buccione [b], Giovanni Mongelli [b], Ouafi Ameur-Zaimeche [a], Olivier Bruguier [c], László Kocsis [d], Rabah Laouar [e]

[a] Laboratoire des Réservoirs Souterrains: Pétroliers, Gaziers et Aquifères, Université de Ouargla, 30000, Algeria
[b] Department of Applied and Basic Sciences, University of Basilicata, 85100 Potenza, Italy
[c] Géosciences Montpellier, Université de Montpellier, CNRS-UMR 5243, Place E. Bataillon, 34095 Montpellier cedex 5, France
[d] Institute of Earth Surface Dynamics, Faculty of Geosciences and Environment, University of Lausanne, Switzerland
[e] Geology department, Faculty of Earth Sciences, University of Badji Mokhtar Annaba, B.P. 12, 23000 Annaba, Algeria

ARTICLE INFO

Keywords:
REE
Matrix
Glauconitization
Phosphorites
Algeria

ABSTRACT

The Algerian phosphorites, deposited during the Paleocene-Eocene, are part of the Tethyan phosphogenesis along the southern paleo-Tethys margin. Located primarily in the Tebessa region, these deposits hold reserves exceeding 2 billion metric tons. Recent interest has grown due to their enrichment in rare earth elements plus yttrium (REY). While previous studies have examined whole-rock and grain-size fractions, the fine-grained matrix (<45 μm) remains poorly explored. This study provides the first mineralogical and geochemical characterization of this fraction to assess its economic potential and paleoenvironmental significance. Twenty-two fine-fraction samples from four Tebessa localities were separated using humid grain-size classification. Mineralogical analysis was supported by X-Ray Powder Diffraction (XRD), whereas geochemical analyses were carried out using inductively coupled plasma optical emission spectroscopy (ICP-OES) and inductively coupled plasma mass spectrometry (ICP-MS).

The XRD results show that the phosphorite fine-grained matrix is composed of calcite, dolomite, carbonate fluorapatite, glauconite, quartz, chlorite, and gypsum. Notably, glauconite occurs in higher amounts in southern deposits (Kef Essenoun), suggesting intensified glauconitization process. Geochemically, the fine fraction contains an average of 12.48 wt% P_2O_5, with REY concentrations ranging from 55 to 863 ppm. REY contents increase southward, with REEs ranging between 68 and 678 ppm (avg. 416 ± 198 ppm) and Y varies from 9 to 187 ppm (avg. 125 ± 56 ppm). The higher REY content is partly linked to glauconite phase abundance. Normalized REY contents indicate seawater-like patterns in the northern deposits, whereas the southern deposits show middle REE (MREE) enrichment patterns. High $(La/Yb)_N$ ratios in the glauconite-rich samples suggest early-diagenetic adsorption under slow sedimentation rate and sub-reduced conditions. An enhanced glauconitization process occurred in the southern basin at the Paleocene–Eocene boundary, which is marked by global thermal event. These findings suggest that the fine-grained matrix, typically considered as waste during the treatment of raw phosphorites, holds economic potential due to its high REY content, presenting a promising resource for future exploitation.

1. Introduction

During the Paleogene period, large amounts of phosphatic matter were deposited in the southern side of the Tethyan Ocean, where these sediments were transformed into phosphorites (Sassi, 1974; Notholt, 1980; Sheldon, 1987; Notholt et al., 1989; Lucas and Prevot-Lucas,

* Corresponding author.
E-mail addresses: aouachria.riadh@univ-ouargla.dz (R. Aouachria), kechiched.rabah@univ-ouargla.dz (R. Kechiched), roberto.buccione@unibas.it (R. Buccione), giovanni.mongelli@unibas.it (G. Mongelli), olivier.bruguier@umontpellier.fr (O. Bruguier), laszlo.kocsis@unil.ch (L. Kocsis), rabah.laouar@univ-annaba.dz (R. Laouar).

https://doi.org/10.1016/j.gexplo.2025.107889
Received 5 May 2025; Received in revised form 22 July 2025; Accepted 27 August 2025
Available online 1 September 2025

1995). The processes leading to the formation of phosphorites is known as phosphogenesis; this results from the overlap of several biological, physical and chemical factors (Krajewski, 1994; Föllmi, 1996; Schulz and Schulz, 2005; Arning et al., 2009; Goldhammer et al., 2011; Brock and Schulz-Vogt, 2011; Ciobotă et al., 2014; Salama et al., 2015; Mänd et al., 2018; Lumiste et al., 2021). The North African realm is known by high amounts of phosphorites, as a part of this phosphogenesis system, and was studied by several authors (e.g. Ounis et al., 2008; Ben Hassen et al., 2009, 2010; Galfati et al., 2010; Garnit et al., 2012, 2017; Kocsis et al., 2013, 2014; Ciobotă et al., 2014; Salama et al., 2015). Particularly, the Algerian and Tunisian phosphorites, which were deposited around Kasserine Island during Cretaceous to Upper Eocene, have gained greater interest in the last decade (Kocsis et al., 2014; Kechiched et al., 2016, 2018, 2020, 2024; Garnit et al., 2017; Bouabdallah et al., 2019; El Zrelli et al., 2019; Ettoumi et al., 2020; Buccione et al., 2021; Dass amiour et al., 2021; Laouar et al., 2024; Diab et al., 2024).

The Algerian phosphorites are located mainly in the Tebessa area, close to the Algerian-Tunisian border. They are located in two distinct basins: the northern basin represented by Djebel El Kouif phosphorites and the southern basin which correspond to the Djebel Onk complex, including Kef Essenoun and Bled El Hadba deposits. These phosphorite deposits were studied by many authors especially for their geochemical characteristics (e.g., Kechiched, 2017; Kechiched et al., 2018, 2020, 2024; Buccione et al., 2021; Dass amiour et al., 2021; Laouar et al., 2024; Diab et al., 2024). Based on these studies, high amounts of REE were recorded, notably in the main layer of phosphorites from the Kef Essenoun deposit (min = 576 ppm; max = 906 ppm, Kechiched et al., 2020). This REE enrichment was partly attributed to abundance of glauconitic particles, which yield marked ∑REE enrichment, exceeding 1000 ppm compared to other phosphatic particles, such as the pellets and coprolites in the phosphorite rock (Kechiched et al., 2018). This was recently confirmed by Laouar et al. (2024) when studying the neighboring Bled El Hadba deposit, where the glauconite particles have been reported to be enriched in the ∑REE more than any other Tethyan deposits (up to 2050 ppm, with an average of 1429 ppm). These authors mentioned the role of the paleoenvironmental conditions in both the REE uptake and the glauconitization processes that affected the phosphatic particles. Furthermore, it was also mentioned that early diagenetic conditions mainly control REE uptake and distribution rather than any other factors, such as seawater chemistry and phosphatic grain-size (Valetich et al., 2022; Ferhaoui et al., 2022).

Using “in situ” analysis on separate particles, the glauconitization process leading to a supplementary enrichment in REE budget was discussed in the light of the geochemical signal (Kechiched et al., 2018; Laouar et al., 2024). However, the mineralogical control was not clearly evidenced, as X-ray diffraction in the whole-rock phosphorites (e.g., Tahri et al., 2019; Kechiched et al., 2020) does not show the presence of glauconite minerals. Laouar et al. (2024) pointed out that glauconite is ‘structurally immature’ according to LA-ICP-MS chemical analysis of the mineral.

The glauconitization effect is worth of investigation, since it involves significant REE enrichment, with an important potential for these critical elements to industry. In addition, the glauconitization process allows to better constrain paleoenvironments and paleoclimate conditions. The glauconite deposits were developed during the Paleogene period in shallow water along continental margins, as a consequence of warm and humid climatic events, also called the global hyperthermal events. The most significant of these is that occurring during the Paleocene-Eocene boundary, known as PETM event (Clay Kelly et al., 1996; Thomas et al., 1999; Bolle et al., 2000; Zachos et al., 2005; Röhl et al., 2007; John et al., 2008; Ferrow et al., 2011; Samanta et al., 2013; Sluijs et al., 2014; Stassen et al., 2015; Banerjee et al., 2016b, 2020; Huggett et al., 2017; Roy Choudhury et al., 2021). This relatively short period is characterized by an unusual increase in sea-surface temperature, sharp sea-level rise, oceanic acidification and ocean deoxygenation (Clay Kelly et al., 1996; Thomas et al., 1999; Bolle et al., 2000; Zachos et al., 2005).

Although geochemical studies on glauconite particle separates and whole-rock samples have provided valuable information in REE distribution and fractionation, studies on phosphate matrix and its role in REE budget are scarce. This matrix, usually reported to be P-depleted, may deliver significant information in tracking glauconitization processes. In the present study, we focus, for the first time, on the phosphorite matrix to characterize its mineralogical and geochemical features. The fine fraction (<45 μm) of the matrix is the target of this study, where four comprehensive phosphorite deposits that belong to both the northern and southern basins of the Tebessa region are investigated.

The main objectives are, therefore, to: (i) characterize the mineralogy of the phosphorite matrix (ii) determine the chemical composition (major, trace and REE contents) of the matrix, (iii) interpret the mineralogical and geochemical results in terms of paleoenvironment and paleoclimate conditions promoting high rate of glauconitization and REY enrichment in the Algerian phosphorites and (iv) preliminary assess the economic significance of the matrix in terms of critical elements.

2. Geological settings

Belonging to the eastern part of the Saharan Atlas, the Tebessa region hosts the main economic deposits of the Algerian phosphorites. These are mainly located in two sub-basins (Fig. 1A): the northern basin includes Djebel El Kouif, Djebel Dyr, Ain Dibba, Ain Kissa and Djebel Tazbant deposits, and the southern basin represented by the Djebel Onk mining district, which includes 5 deposits (Onk Nord, Kef Essenoun (now under open-pit exploitation), Djebel Djemi-Djema, Bled El-Hadba (under extensive exploration), and Oued Btita).

These sedimentary phosphorites were deposited as a result of marine phosphogenesis processes that took place along the southern part of the Tethys Paleo-Ocean margins, during the late Cretaceous to the early Paleogene. This process extends geographically from North Africa to the Middle East, (Sassi, 1974; Notholt, 1980; Sheldon, 1987; Notholt et al., 1989; Lucas and Prevot-Lucas, 1995; Ciobotă et al., 2014; Salama et al., 2015). Large areas in the northern Africa were particularly covered by the Tethys Ocean during the late Paleocene to the early Eocene (~56 Ma), except some emerged islands, such as the Kasserine and the Djeffara Islands (Fig. 1B) (Sassi, 1974; Burollet and Oudin, 1980; Fourine, 1980). On the Kasserine Island borders, giant amounts of phosphatic matter, carried by the Tethys upwellings, were deposited (Sassi, 1974; Burollet and Oudin, 1980; Fourine, 1980). Three basins were, then, formed around this island, including: (i) Sra Outran basin in the north (the northern basin), (ii) Gafssa-Metlaoui basin in the south (the southern basin) and (iii) Meknassi-Mezzouna basin in the east (the eastern basin) (Zaïer, 1984; Chabou-Mostefai, 1987; Beji-Sassi and Sassi, 1999).

In this study, the investigated deposits belong to the Algerian realm westerward of this paleo-island, and are represented by (1) the Djebel El Kouif and Djebel Dyr phosphorite deposits in the north (Fig. 2A), which belong to the northern basin that extend easterly to Sra Ouartan in Tunisia, and (2) the Kef Essenoun deposit (Djebel Onk, complex) (Fig. 2B) that belongs to the Gafsa-Metlaoui-Onk southern basin (e.g., Chabou-Mostefai, 1987; Kechiched et al., 2024). In both areas, the sedimentary rocks were deposited during the Mesozoic-Cenozoic times (Fig. 2) (Dubourdieu, 1956; Durozoy, 1956; Blès and Fleury, 1971). The studied phosphorites in the northern basin consist of several decimeter- to meter-thick levels - (Blès and Fleury, 1971; Kechiched et al., 2020) (Fig. 3), whereas, those of the southern basin often show a single layer that may reach 35 m in thickness (Cielensky et al., 1988; Kechiched et al., 2020) (Fig. 4C-D).

The petrological features of the studied deposits have already been detailed by a number of authors (e.g., Chabou-Mostefai, 1987; Kechiched et al., 2020). Here, we provide a brief overview of the phosphorite layers. For *the northern sites*, the lithological units in the Djebel Dyr (Fig. 3B) are mostly composed of limestones, marls and

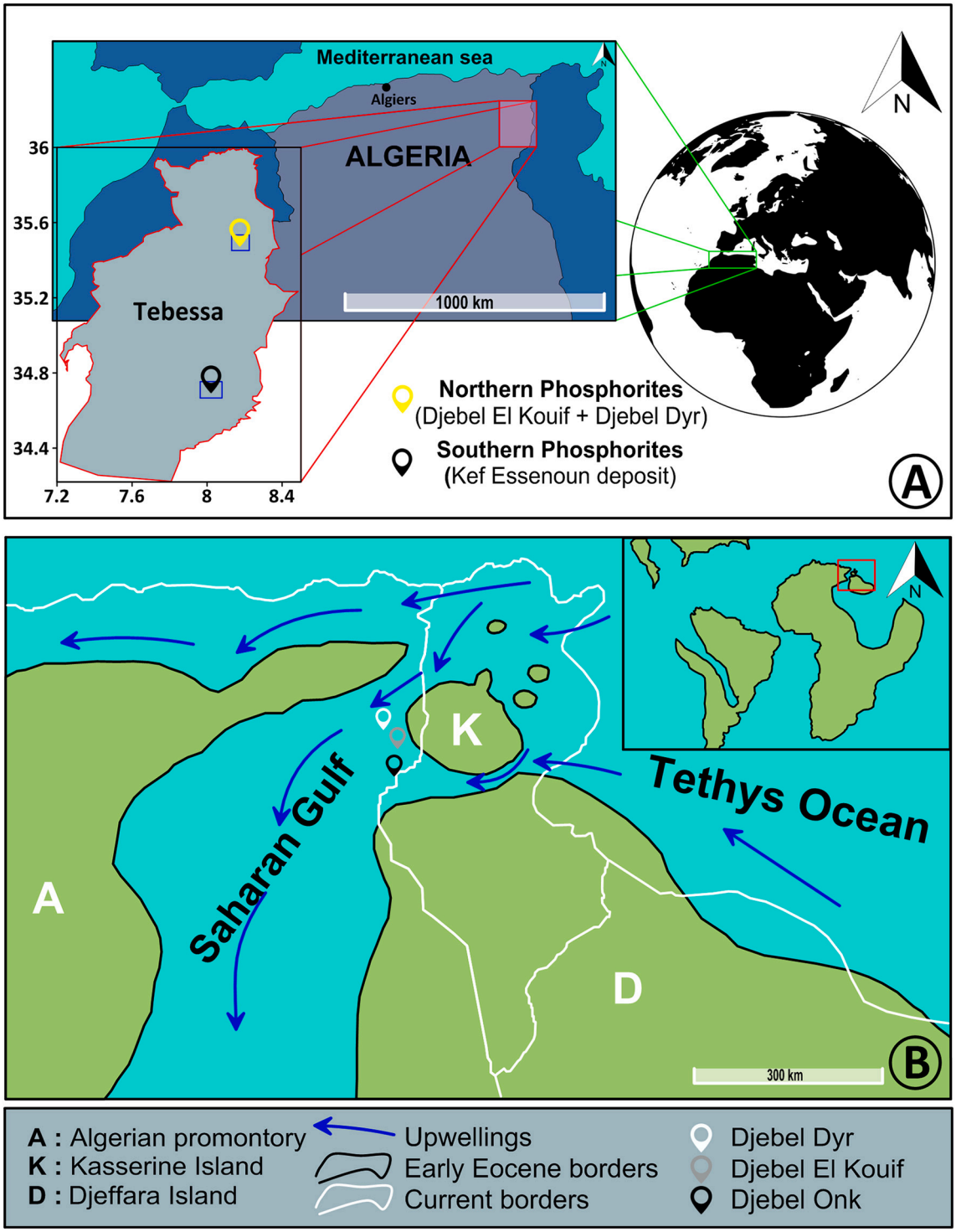

Fig. 1. (A) Geographical position of the Algerian Phosphorites in the north of Africa. (B) Paleogeographic map of the Algero-Tunisian phosphorites during the early Eocene (modified after Sassi, 1974; Burollet and Oudin, 1980; Winnock, 1980; Chaabani, 1995; Zaïer et al., 1998).

dolomitic limestones containing thin (10–60 cm) phosphorite levels (Fig. 3A). In the Djebel El Kouif deposit, the studied section is subdivided into three units, based on facies features; from the bottom to the top: (i) Unit A showing marly to clayey, glauconite-rich phosphorites (Fig. 3A), (ii) Unit B displaying grey, medium-grained phosphorites, and (iii) Unit C consisting of cherty phosphorites (Fig. 3A). The Kef Essenoun phosphorites of *the southern basin*, are composed of a single layer that is subdivided into three main sub-layers: (i) Basal sub-layer (Fig. 4a) consisting of ~2 m thick marly phosphorites, alternating with thin dolomite layers, (ii) Main, ~25–30 m thick, sub-layer, which is composed of pellet- and glauconite-rich phosphorites (Fig. 4b-c), and (iii) Upper, 1 to 10 m thick sub-layer consiting of dolomitic phosphorites, with low phosphatic particle contents (Fig. 4d).

3. Sampling, analytical techniques and methodology

For analytical procedures, twenty-two phosphorite samples were collected from the three deposits: 5 samples from Djebel El Kouif and 3

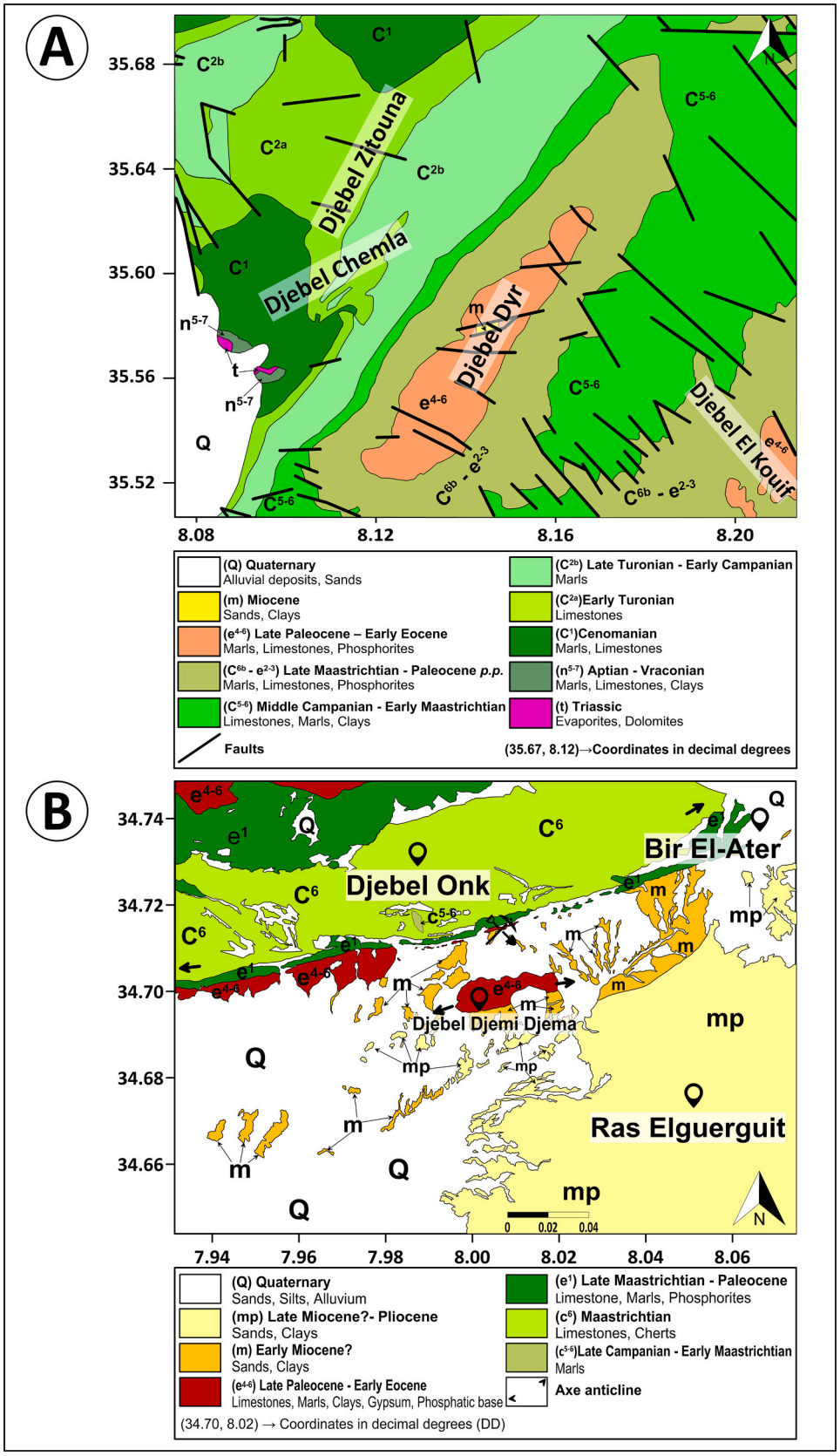

Fig. 2. (A) Geological sketch map of Djebel El Kouif and Djebel Dyr region (from the Geological map of Morsott N°178 (1/50,000) (after Blès and Fleury, 1971). (B) Geological sketch map of Kef Essenoun (from the Geological map of Bir El-Ater N°327 (1/50,000) modified by (ORGM, 2000)).

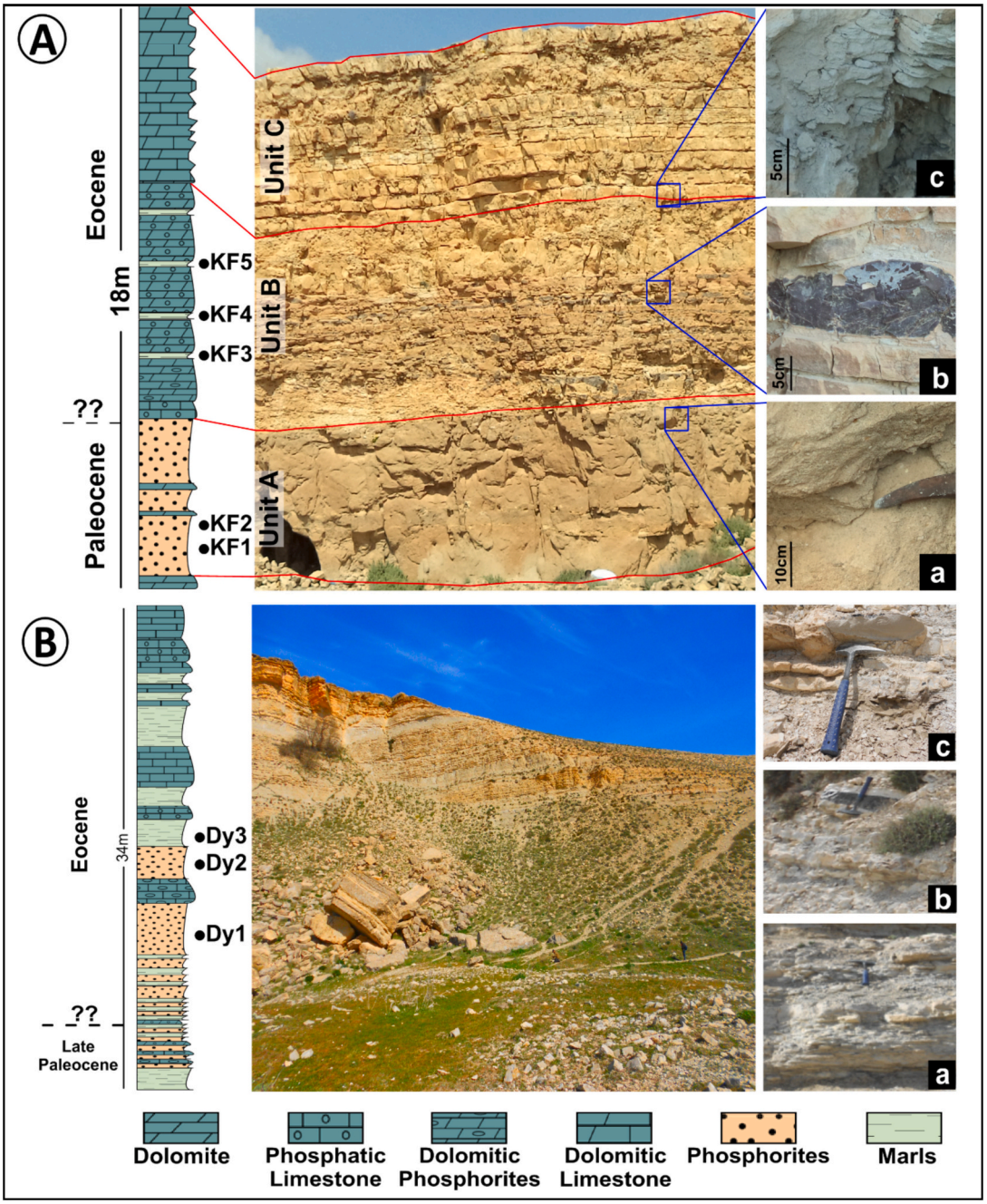

Fig. 3. (A) Field photographs of phosphorites from Djebel El Kouif with lithological column showing sampling position. a- heterogeneous phosphorite. b- chert. c- marl. (B) Field photographs of phosphorites from Djebel Dyr with lithological column showing sampling position. a- greyish marly phosphorites. b- marly phosphorites. c- marl with thin levels of cherty limestone.

samples from Djebel Dyr, grouped in this study as the northern basin phosphorites, and 14 samples distributed in two profiles through the Kef Essenoun deposit representing the southern basin phosphorites. Careful sampling was conducted in order to be representative of all phosphatic lithologies on one hand, and, on the other hand to ensure a comprehensive investigation of the studied material (see the stratigraphic columns on Figs. 3–4). Phosphorite particles were separated from the whole-rock through, crushing, washing and hand-picking techniques, and studied using a binocular microscope. Furthermore, thin sections were also prepared on whole-rocks for petrographic investigation using a transmitted and reflected light optical microscope.

The fine fraction (<45 μm) of the phosphorite matrix was extracted from the whole-rock by a humid grain-size classification method using distilled water. The <45 μm sub-samples, after air-drying, were mineralogically analyzed using X-ray powder diffraction (XRPD) technique at the Department of Basic and Applied Sciences, University of Basilicata, Italy. A Siemens D5000 powder diffractometer with Cu-Kα radiation and a 40 kV, 32 mA, and 0.02° (2θ) step size setup was used. Analyses were performed between 0° and 70° 2θ, using a step size of 0.02° and scan speed of 2 s. The X'Pert HighScorePlus software package (PANalytical_2004) and PDF-2 (2003) data base were used to identify mineral phases. The intensity level is related to the amount of each diffraction peak, which is used to evaluate quantification of mineral compositions.

Major and trace element (including rare earth elements (REE)) concentrations were determined using inductively coupled plasma optical emission spectroscopy (ICP-OES) and inductively coupled plasma

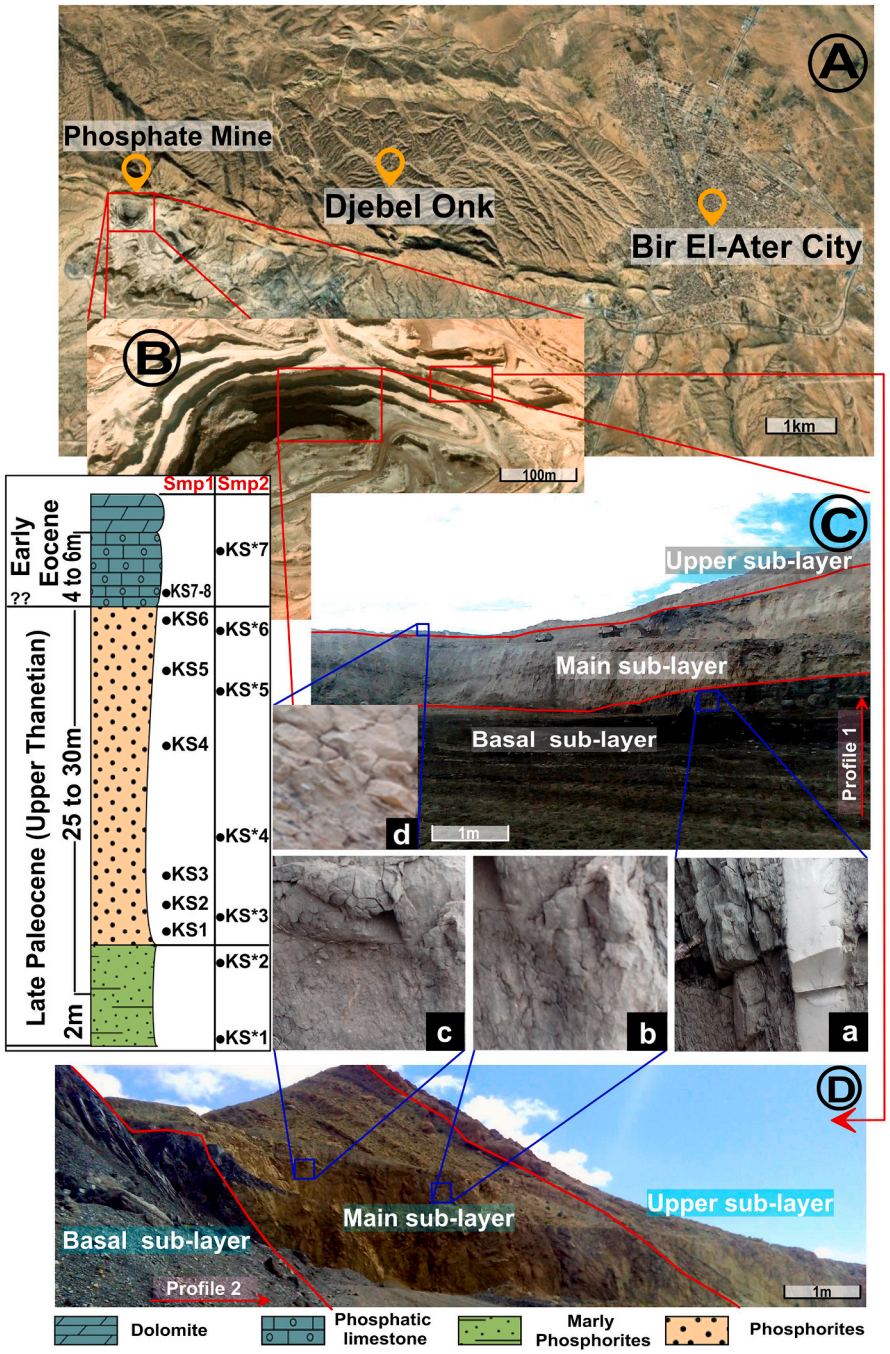

Fig. 4. A) Satellite view (Google earth map) of Djebel Onk and Bir El-Ater region. (B) Zoom on the satellite view of the Djebel Onk phosphate mining complex. (C)-(D) Panoramic view inside the phosphate mine of Djebel Onk. a,b,c, and d: Field photographs of phosphorites from Kef Essenoun deposit: a- marls. b-c- phosphorites. d- limestones.

mass spectrometry (ICP-MS) at Activation Laboratories (Ancaster, Canada), following acid digestion of sample powders (HF, $HClO_4$, HNO_3, and HCl). A 0.25 g of each sample was initially digested in hydrofluoric acid, followed by a mixture of nitric and perchloric acids. Analytical uncertainties were below ±5 %, with uncertainties for elements at concentrations ≤10 mg/kg ranging from ±5–10 %. Loss on Ignition (L.O.I.) was determined by heating the samples overnight at 950 °C.

The one-way ANOVA method was utilized to check if there were any significant differences in the mineralogical and geochemical composition among samples from the northern and southern basins, as well as between the sub-layers of the Kef Essenoun deposit. Compositional data analysis (CoDa), in conjunction with classical statistical methods, is a robust tool to enhance the understanding of elemental relationships and the geochemical processes controlling these relationships (Thiombane et al., 2018; Somma et al., 2021). In this study, a hierarchical clustering algorithm (HCA) was employed using the CoDa approach. For the reliable implementation of both CoDa and statistical analysis, it was critical to work with a dataset free from values below detection limits, therefore elements with non-detected values were replaced by the value of the detection limit. The HCA employed the "Pearson correlation coefficient" to depict any similarity between variables and samples, while for agglomerative clustering, "Unweighted pair-group average" method were used. The clr-transformation was conducted by the CoDa Pack software (Comas-Cufí and Thió-Henestrosa, 2011), whereas the HCA

and statistical tests were carried out using the XLSTAT software (Addinsoft, 2021).

Rare earth elements in this study were subdivided into three groups: light rare earth elements (LREE; from La to Nd), middle rare earth elements (MREE; from Sm to Dy) and heavy rare earth elements (HREE; from Ho to Lu) (e.g., Jaireth et al., 2014).

Cerium anomaly was calculated using the formula proposed by Wright et al. (1987), where Ce/Ce* was derived as $3Ce_N/2La_N + Nd_N$. To evaluate the amplitude of Ce anomaly, Ce_{an} was determined as the logarithm of the Ce/Ce* ratio. Eu/Eu* ratios were calculated using the Taylor and McLennan (1985) formula, expressed as $Eu/Eu^* = Eu_N/(Sm_N \times Gd_N)^{0.5}$. Pr/Pr* ratio was determined from the formula $2Pr_N/(Ce_N + Nd_N)$ given by Bau and Dulski (1996). The Y anomaly (Y/Y*) was calculated using the formula of Fazio et al. (2007) as $Y/Y^* = 2Y_N/(Dy_N + Ho_N)$. N refers to PAAS-normalized elements.

To evaluate the economic significance of REE plus Yttrium (hereafter REY), the REY coefficient outlook (C_{outl}), proposed by Seredin (2010) and extensively used by some authors (e.g., Buccione et al., 2021; Ferhaoui et al., 2022; Laouar et al., 2024), was applied in this study. The C_{outl} ratio is calculated as $(Nd + Eu + Tb + Dy + Er + Y)/\sum REE)/(Ce + Ho + Tm + Yb + Lu)/\sum REE)$. Additionally, the percentage of critical elements (REY_{def}) within the total REY content in the analyzed fractions is determined based on the quantities of individual critical and potentially critical REY elements. Furthermore, the economic importance (EI)

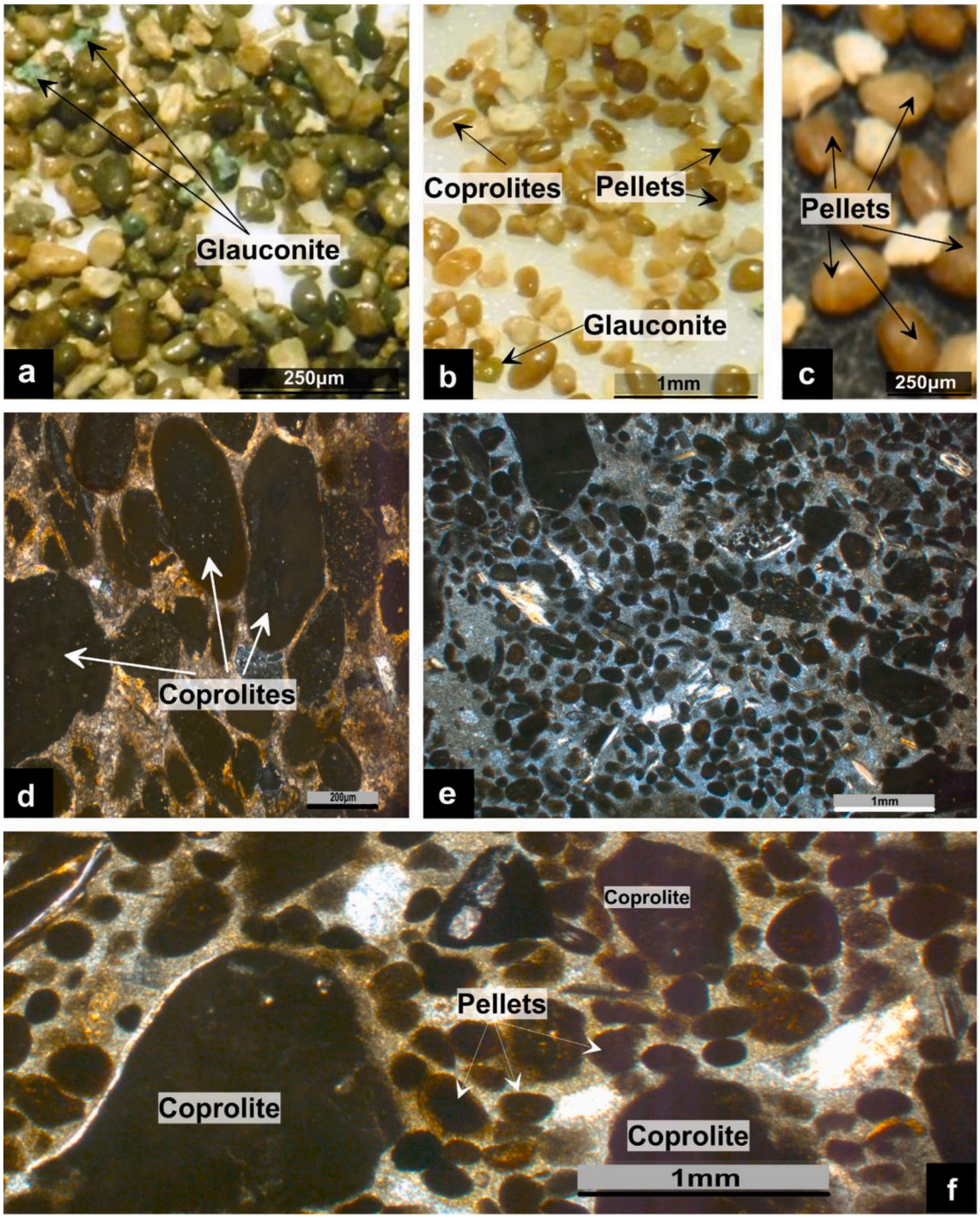

Fig. 5. a-c- Particles' separates and d-f- thin sections showing the main phosphate particles from the two studied basins.

and the supply risk (SR), as defined by Grohol and Veeh (2023), and related ratios, were applied.

4. Results

4.1. Petrographic features

Whole-rock phosphorite samples are composed of phosphatic particles, including coprolites, pellets, bone fragments, and glauconites that are cemented by clayey, marly and/or carbonate matrix (Fig. 5). The coprolites are often cylindrical particle of ~0.5 to 1 mm in diameter, preserving the original form of fecal material, showing yellowish-brown to creamy colors (Fig. 5B). The pellets, however, are often well smoothed particles of ~0.2 mm in diameter (Fig. 5B). The glauconites, of a diameter similar to that of the pellets, are more abundant in the southern basin and are easily distinguished by their greenish color (Fig. 5A). The fine-grained fraction of the matrix, investigated in this study, is more calcareous in the northern basin deposits than in the southern basin Kef Essenoun phosphorites, where it displays relatively clayey-rich nature in both investigated profiles. The upper sub-layer, however, displays enrichment of siliceous matrix (Fig. 5E).

4.2. Mineralogical composition

The X-ray diffraction analyses of the fine fraction (< 45 μm) from the phosphorites of both the northern and southern basins reveal generally similar mineralogical phases (Fig. 6; Table 1, Supplementary materials). However, notable variations in the quantities of these phases are observed in space (between the two sectors) and in time (along the vertical profiles). The main mineral among all is the carbonate fluorapatite (CFA) (d-spacing = 2.78 Å), associated with dolomite (d-spacing = 2.89 Å), glauconite (d-spacing = 9.05 Å), quartz (d-spacing = 3.34 Å), chlorite (d-spacing = 14.01 Å) and gypsum (d-spacing = 7.63 Å) (Fig. 6).

Considering the semi-quantitative abundance of mineralogical phases between the two studied phosphorite basins, the northern deposits show abundant dolomite in Djebel El Kouif (average = ~ 67 %) and calcite in Djebel Dyr (average = ~ 68 %). The accessory minerals are represented by glauconite ranging from ~6 % to ~11 % (average = 8 ± 2 %), CFA (from ~14 to ~23 %), quartz (~5 % to ~21 %), and chlorite (~7 % to ~11 %). Conversely, the southern deposits are marked by a dominance of dolomite varying from ~10 % to ~81 % (average = ~41 % ± 24 %), glauconite ranging from ~8 % to 61 % (average = ~28 ± 18 %) and calcite (~ 19 % to 47 %, average 38 % ± 16 %). The fine fraction in these deposits exhibits lesser amounts of CFA ranging from ~8 % to ~33 % (average = ~22 ± 8 %). Slight presence of gypsum (average = ~10 % ± 5 %) was also recorded.

The vertical distribution of mineralogical phase proportions within the fine fraction of the studied sections is shown in Table 1. Notably, the distribution exhibits a marked variation from the base to the top of the studied profiles, particularly for glauconite. At the northern basin, at Djebel Dyr and in, a lesser degree, at Djebel El Kouif, glauconite is relatively scarce, except some levels where the contents can reach ~6 to ~11 %. Remarkably, at the Kef Essenoun sections, glauconite is more abundant and displays significant vertical variability. For instance, the glauconite amounts can reach the highest content 61 % towards the upper section compared to the lower section (Fig. 6; Table. 1). For other mineral phases, they fluctuate vertically according to the nature of the phosphorite facies. The CFA is present in the matrix with relatively higher amounts, as a result of P-enriched facies, particularly in the main sub-layer (up to ~33 %) compared to the basal sub-layer (~12 % at most). Conversely, dolomite displays the highest amounts at the basal sub-layer (~81 %) correlate negatively with P-contents of the facies in both basins. Regarding the presence of calcite, the highest amounts were recorded in the top of Djebel Dyr section (up to 73 %), while gypsum and chlorite are rare.

4.3. Geochemistry

The major, trace and rare earth element compositions of the analyzed matrix samples are reported in Tables 2 and 3 for the northern and southern basin respectively.

4.3.1. Major elements

For major element compositions, the results show a dominance of CaO varying between 13.7 and 38.73 wt%, with an average of 30.75 ± 6.51 wt% in almost all samples, except for samples KS1, KS2, KF3, and Dy3 where the SiO_2 dominate with concentrations ranging from 27.24 to 39.00 wt%. P_2O_5, in the second dominant element, showing values from 0.79 to 17.64 wt% in the northern basin, and from 0.9 wt% to 22.24 wt% in the southern basin. MgO values range from 1.64 to 9.52 wt%, with relative enrichment in the northern deposits (average = 6.88 ± 2.09 wt %). The samples display low K_2O and Fe_2O_3 contents (0.32–1.79 wt%, and 0.43–2.85 wt% respectively), while high values are reported in glauconite-rich levels. Al_2O_3 shows higher contents than those of Fe_2O_3 and K_2O (ranging from 2.03 to 7.43 wt%). The remaining of major elements show lower contents, such as MnO (≤ 0.03 wt%) and TiO_2 (≤ 0.31 wt%).

When comparing the northern and southern basin phosphorite matrices, the northern deposits are depleted in P_2O_5 (average = 8.30 ± 6.51 wt%) compared to southern deposits (average = 14.87 ± 5.77 wt %) (Fig. 7A). Similarly, SiO_2, Al_2O_3, and K_2O contents are depleted (average values of 18.08 ± 8.94 wt%, 3.24 ± 1.22 wt%, and 0.52 ± 0.17 wt%, respectively), relative to those of the Kef Essenoun sections, which show averages of 21.01 ± 8.63 wt%, 4.42 ± 1.66 wt%, and 0.88 ± 0.34 wt%, respectively. (Fig. 7A).

4.3.2. Trace elements composition

The Most abundant trace element contents, with decreasing order are Sr, Cr, Zn, Y, V, Ba, Ni, Zr and Cu, with Sr having the highest concentration (up to 2010 ppm). This trend is similar in both basins (Fig. 7B). In the Kef Essenoun deposit, the samples from both profiles show the highest Sr concentrations (212 to 2010 ppm; average = 1336 ± 491 ppm), followed by Cr (170 to 1220 ppm; average = 665 ± 278 ppm) (Fig. 7B). Conversely, at Djebel El Kouif, Cr displays higher contents (from 660 to 1780 ppm; average = 1208 ± 432.4 ppm) in all samples compared to those of Sr (from 579 to 1169 ppm; average = 850 ± 244 ppm) (Fig. 7B).

Despite the vertical fluctuation of trace elements contents, the one-way ANOVA analysis reveals a significant variation in some elements between the northern and southern basins, such V ($p = 0.025$), Ni ($p = 0.043$), Cu ($p = 0.011$), Mo ($p = 0.026$), Ti ($p = 0.008$). For instance, V, Ni, and Cu are relatively enriched in northern deposits (with averages of 537 ppm, 120 ppm, 37 ppm, respectively) compared to southern samples (averages: 229 ppm, 64 ppm, 20 ppm, respectively) (Fig. 7B). On the other hand, the northern sectors are depleted in Mo and Ti, with average values of 3 ppm and 0.38 ppm respectively, compared to those of southern Kef Essenoun deposit (averages: Mo = 17 ppm, Ti = 7 ppm). The trace elements, such as Cr, Ba, Y, and Zn, show relatively similar variation ($p > 0.05$) (Fig. 7B) in both basins, although the vertical trend of these elements is not uniform and may show positive or negative shifts vertically. The remaining trace elements, such as Sc, Be, Co, Ga, Ge, As, Nb, Ag, In, Sn, Sb, Cs, Hf, Ta, W, Tl, Pb and Bi, display low contents (less than 10 ppm).

4.3.3. Rare earth elements composition

From Table 2 and Table 3, it can be seen that the sum of rare earth elements ∑REE in the southern basin (68 ppm to 678 ppm; average = 416 ± 198 ppm) is three times greater than that recorded in the northern basin, with contents ranging from 41 to 316 ppm (average = 142 ± 109 ppm) (Fig. 7C; Tables 2–3). Similarly, Y contents are relatively enriched in southern deposits, varying from 9 to 187 ppm (average = 125 ± 56 ppm), compared to those of the northern basin (14 to 210 ppm, average

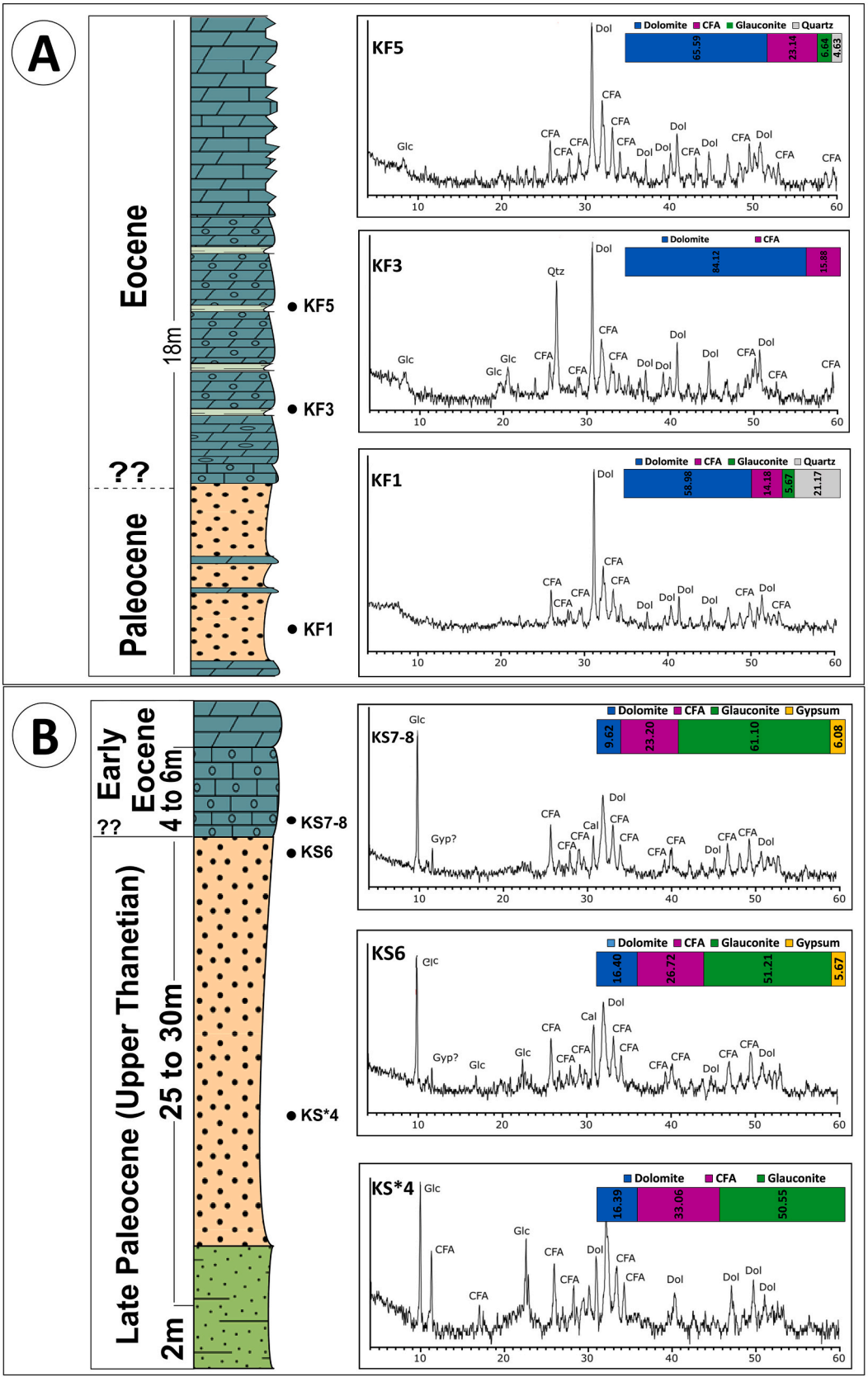

Fig. 6. Representative XRPD patterns of the phosphorite matrix samples from the northern and southern basin phosphorites. (A) Djebel El Kouif, (B) Kef Essenoun, CFA = carbonate fluor-apatite, Dol = dolomite, Cal = calcite, Qtz = quartz, Gyp = gypsum, Glc = glauconite.

Table 1
Vertical variation of the matrix mineralogical composition of samples from the northern and southern basin phosphorites. Cal = calcite, Dol = dolomite, CFA = carbonate fluor-apatite, Qtz = quartz, Chl = Chlorite, Glc = Glauconite, Gyp = gypsum.
(>60 %) •••• Abundant, (40–60 %) ••• High, (20–40 %) •• Moderate, (5–20 %) • Low, (<5 %) rare.

Locality	Samples	Age	Cal	Dol	CFA	Qz	Cht	Glt	Gyp
Northern Deposits	**El Kouif**								
	KF5	Paleocene - Eocene		••••	••			•	
	KF4			•••	•	•		•	•
	KF3			•••	•	••		•	
	KF2			••••	••		•		
	KF1			••••	•				
	Djebel Dyr								
	Dy3	Paleocene - Eocene	••••		•			•	
	Dy2		••••		•			•	
	Dy1		••••		•		•	•	
Southern deposits	**Kef Essenoun (Profil 1)**								
	KFS7-8	Paleocene - Eocene		•	••			••••	•
	KFS6			•	••			•••	•
	KFS5			•••	•			••	
	KFS4			••	••			••	•
	KFS3			•••	••			•	
	KFS2			••	••			••	•
	KFS1			••••	••			•	
	Kef Essenoun (Profil 2)								
	KS*7	Paleocene - Eocene	•	•••	••		•		
	KS*6			••••	••				
	KS*5			•••	••		•	••	
	KS*4			•	••			•••	
	KS*3		•••	•	•			•	
	KS*2		•••	•	•		•	•	•
	KS*1			••••			•	•	

(>60%) •••• Abundant , (40-60%) ••• High , (20-40%) •• Moderate , (5-20%) • Low , (<5%) rare

= 88 ± 77 ppm). Light rare earth elements "LREE" (La—Nd) are the most abundant class among the REE in both basins. However, in the southern basin, the contents are much higher (59 to 554 ppm, average = 339 ± 162 ppm) than those observed in the northern basin (ranging from 34 to 225 ppm, average = 104 ± 75 ppm) (Fig. 7C; Tables 2–3). Middle rare earth elements "MREE" (Sm—Dy) are relatively enriched in southern basin (7 to 92 ppm, average = 56.96 ± 27.66 ppm) relative to those recorded in the northern basin, with concentrations ranging from 5 to 58 ppm (average = 24 ± 21 ppm) (Fig. 7C; Tables 2–3). Heavy rare earth elements "HREE" (Ho—Lu) display the lowest contents in both basins, with averages of 21 ± 9.14 ppm in Kef Essenoun and 14 ± 12 ppm in the northern phosphorites (Fig. 7C; Tables 2–3).

To evaluate the fractionation between the three REE groups, the $(La/Yb)_N$ and $(Gd/Yb)_N$ ratios were used. The northern basins show low values of $(La/Yb)_N$, ranging from 0.59 to 0.94 (average = 0.69 ± 0.12) compared to those of the southern basin phosphorites (0.76 to 1.39; average = 1.04 ± 0.13). Regarding to the $(Gd/Yb)_N$ ratios, the northern basins show lower values ranging from 0.74 to 0.98 (average = 0.89 ± 0.07), while the southern basin exhibits higher values (from 1.09 to 1.66; average = 1.49 ± 0.18).

Cerium anomaly (expressed as log Ce/Ce*) shows relatively lower values, ranging from −0.65 to −0.26 (average = −0.44 ± 0.16), in northern basin compared to those registered in the southern basin phosphorites (from −0.38 to −0.09; average = −0.19 ± 0.06). Europium anomaly (expressed as Eu/Eu*) range from 0.99 to 1.18 (average = 1.09 ± 0.07) in the northern sites, whereas in the Kef Essenoun phosphorites, the values are much higher, ranging from 1.09 to 1.2 with an average of 1.13 ± 0.04. Y anomaly (expressed as Y/Y*) displays values ranging from 1.55 to 2.37, with an average of 1.85 ± 0.28 in northern basin. These are clearly higher than those recorded in the southern basin (min = 0.97; max = 1.78; average = 1.48 ± 0.18).

4.4. Geochemical clusters and REE-controls

The relationships between the different variables, including correlations, are constrained, and no single element can vary independently of the others in the composition. In the present study, the method used for the hierarchical clustering algorithm (HCA) is coupled with CoDA. In this approach, raw data were converted into centered log ratio (clr) following Aitchison's rules (Aitchison, 1986), as well as several studies on compositional data analysis (CoDa), such as that of Ebrahimi et al. (2021). The HCA results, presented in Fig. 8, provide an overview of the relationships between various geochemical variables and samples.

For variable clustering, the dendrogram (Fig. 8A) delineates two main clusters. Cluster 1, which reflects CFA minerals and associated elements, is subdivided into two sub-clusters: the first comprises As, Ag, and Sb, grouped with Ti, Th, and LREE, whereas the second, includes MREE and HREE, U, Sr, Y, along with and P_2O_5, Na_2O. Cluster 2 is subdivided into three sub-clusters. The first, which represents the matrix phase (calcareous and clays), consists of major oxides such as CaO, MgO, SiO_2, Al_2O_3, Fe_2O_3, MnO, and TiO_2, along with several trace elements, including Be, Rb, Cs, Nb, Ta, Sc, and Pb; the second is associated with productivity indicators and precursor elements, encompassing Cr, Ba, Cu, V, and Zn; and the third sub-cluster comprises K_2O and Mo, which may be linked to the clay-rich fraction of the matrix.

Dendrogram B (Fig. 8B), which clusters the samples, displays two main groups. The first group includes samples characterized by high glauconite amounts and high ∑REE concentration (up to 678 ppm), predominantly from the southern basin, whereas the second cluster consists glauconite- and subsequently REE-depleted samples, mainly from northern deposits.

Table 2
Whole-rock major, trace and rare earth element contents of phosphorite matrix from the northern basin phosphorites.

Samples	KF1	KF2	KF3	KF4	KF5	Dy1	Dy2	Dy3
Locality	Djebel El Kouif					Djebel Dyr		
Major elements (wt%)								
SiO_2	10.02	13.37	27.24	20.98	8.7	15.26	14.52	34.56
Al_2O_3	2.26	2.87	3.33	5.22	2.03	2.73	2.46	5.01
Fe_2O_3(T)	1.63	2.08	1.76	1.84	0.67	1.07	0.89	2.17
MnO	0.027	0.032	0.03	0.02	0.015	0.009	0.009	0.023
MgO	6.21	6.87	7.96	9.52	8.83	4.72	7.66	3.29
CaO	36.06	31.9	25.39	25.4	36.59	35.51	32.79	24.22
Na_2O	1.29	1.47	0.7	0.7	0.96	0.32	0.44	0.48
K_2O	0.34	0.4	0.49	0.84	0.32	0.56	0.55	0.64
TiO_2	0.156	0.177	0.193	0.278	0.116	0.173	0.144	0.297
P_2O_5	17.64	14.57	8.73	7.37	13.6	1.07	0.79	2.63
CaO/P_2O_5	2.044	2.189	2.908	3.446	2.690	33.187	41.506	9.209
Cu/Al_2O_3	26.549	24.390	12.012	7.663	14.778	7.326	8.130	3.992
Trace elements (ppm)								
Sc	11	12	4	6	3	3	3	6
Be	2	2	1	2	< 1	< 1	< 1	2
V	1156	1172	356	492	670	162	176	111
Ba	425	79	69	57	33	33	30	55
Sr	1169	974	637	579	891	660	595	602
Y	210	202	55	77	91	20	14	38
Zr	53	55	50	66	38	40	38	85
Cr	1440	1780	660	1210	950	240	200	270
Co	6	8	1	3	2	< 1	< 1	3
Ni	240	260	130	70	50	80	70	60
Cu	60	70	40	40	30	20	20	20
Zn	1150	1150	650	290	160	150	150	220
Ga	10	13	6	7	4	5	4	7
Ge	< 1	< 1	< 1	< 1	< 1	< 1	< 1	< 1
As	6	5	< 5	5	< 5	< 5	< 5	< 5
Rb	9	11	16	28	10	15	15	25
Nb	6	6	5	9	4	7	6	10
Mo	< 2	< 2	2	< 2	< 2	2	< 2	4
Ag	3.4	5.4	1.6	1.3	1.3	1.6	1.4	2
In	< 0.2	< 0.2	< 0.2	< 0.2	< 0.2	< 0.2	< 0.2	< 0.2
Sn	1	1	1	1	< 1	1	< 1	1
Sb	2.6	1.4	1.3	0.8	< 0.5	< 0.5	< 0.5	< 0.5
Cs	0.6	0.6	1	1.7	0.6	0.8	0.9	1.8
Hf	1.4	1.6	1.2	1.7	0.9	0.9	0.9	1.8
Ta	0.5	0.5	0.4	0.6	0.4	0.4	0.4	0.7
W	7	16	< 1	< 1	< 1	< 1	< 1	< 1
Tl	0.3	0.3	0.6	0.3	< 0.1	< 0.1	< 0.1	0.4
Pb	6	7	< 5	7	< 5	< 5	< 5	< 5
Bi	< 0.4	< 0.4	< 0.4	< 0.4	< 0.4	< 0.4	< 0.4	< 0.4
Th	4.1	5.1	2.3	3.5	1.7	1.7	1.7	3.2
U	78.3	73.7	23.1	26.1	42.7	9.6	5.1	9.8
Rare earth elements (ppm)								
La	98.5	93.6	27	37.6	35.8	14.3	11.4	24.5
Ce	43	42.9	20.6	28.4	17.5	13.2	12.2	25.1
Pr	15.4	15	4.12	5.69	4.75	2.42	1.99	4.57
Nd	67.8	66.6	17.1	23.8	20.4	9.6	8.1	19.5
Sm	14	13.8	3.2	4.9	3.9	1.9	1.5	3.8
Eu	3.67	3.76	0.81	1.14	1	0.49	0.34	1
Gd	18.1	17.7	4.3	6	5.5	2.1	1.4	4.2
Tb	3	2.9	0.7	1	0.9	0.3	0.2	0.7
Dy	18.8	18.5	4.3	6.1	6.2	2.1	1.5	4.2
Ho	4.4	4.4	1.1	1.5	1.5	0.5	0.3	0.9
Er	13.5	13.5	3.4	4.5	5	1.5	1	2.7
Tm	1.88	1.82	0.48	0.66	0.71	0.22	0.14	0.41
Yb	11.8	11.7	3.1	4.2	4.5	1.4	0.9	2.6
Lu	2.07	1.94	0.53	0.73	0.76	0.22	0.14	0.42
REEs	315.92	308.12	90.74	126.22	108.42	50.25	41.11	94.6
REY	525.92	510.12	145.74	203.22	199.42	70.25	55.11	132.6
LREE (La—Nd)	224.7	218.1	68.82	95.49	78.45	39.52	33.69	73.67
MREE (Sm—Dy)	57.57	56.66	13.31	19.14	17.5	6.89	4.94	13.9
HREE (Ho—Lu)	33.65	33.36	8.61	11.59	12.47	3.84	2.48	7.03
(La/Nd)N	1.289	1.247	1.401	1.402	1.557	1.322	1.249	1.115
(Sm/Yb)N	0.603	0.599	0.524	0.593	0.440	0.690	0.847	0.743
(Sm/Pr)N	1.446	1.464	1.236	1.370	1.306	1.249	1.199	1.323
(La/Sm)N	1.022	0.985	1.226	1.115	1.334	1.093	1.104	0.937
(La/Yb)N	0.616	0.591	0.643	0.661	0.587	0.754	0.935	0.696

(*continued on next page*)

Table 2 (*continued*)

Samples	KF1	KF2	KF3	KF4	KF5	Dy1	Dy2	Dy3
Locality	Djebel El Kouif					Djebel Dyr		
(Gd/Yb)N	0.928	0.915	0.839	0.865	0.740	0.908	0.941	0.978
Eu/Eu*	1.086	1.133	1.028	0.990	1.017	1.155	1.105	1.179
Pr/Pr*	1.373	1.357	1.223	1.217	1.309	1.221	1.149	1.162
Ce/Ce*	0.226	0.236	0.405	0.401	0.266	0.482	0.550	0.509
Ce anomaly	−0.645	−0.628	−0.393	−0.397	−0.575	−0.317	−0.260	−0.293
Y/Y*	1.839	1.783	2.008	2.025	2.375	1.554	1.664	1.559
Y/Ho	47.727	45.909	50.000	51.333	60.667	40.000	46.667	42.222

5. Discussion

5.1. Texture and mineralogy: Clues for glauconitization

Petrographic investigations from both the northern and southern basin phosphorites show that phosphatic particles are generally of fecal origin (e.g., Kechiched et al., 2020), consisting of pellets and coprolites. The smooth, well-polished surfaces of the pellets from the southern deposits indicate transport processes (Chabou-Mostefai, 1987; Ben Hassen et al., 2010; Kechiched et al., 2018, 2020), resulting in higher pellet content in this basin phosphorites. Previous SEM-EDS investigations (e.g., Dass Amiour et al., 2013; Kechiched et al., 2020) highlighted the porous structure of these particles, which provides a favorable environment for glauconite formation (Pryor, 1975; Odin and Matter, 1981; Glenn and Arthur, 1988; Chafetz and Reid, 2000; Chattoraj et al., 2016).

Also, several petrographic studies highlight significant enrichment of glauconitic particles in the southern deposits (e.g., Kef Essenoun; Kechiched et al., 2018, and Bled El Hadba; Laouar et al., 2024). However, whole-rock mineralogical observation (XRD analyses) did not show any evidence of the glauconite mineral, most likely due to its low abundance (< 5 %). Laouar et al. (2024) attribute this absence in X-ray patterns to its 'structural immaturity' indicating that the number of cations in its structural formula is incomplete. Focusing the XRD analysis on the fine fraction, where glauconitic phase is concentrated, this enables glauconite detection in XRD patterns (see Fig. 6), with contents ranging from 8 % to 61 % and significant variations between the northern and southern basins (p-value <0.02). This mineral is notably present in the basal levels of the Djebel El Kouif phosphorites and the main sub-layer of the Kef Essenoun deposit, which, based on lithological correlations (Kechiched et al., 2024), appear to correspond to the Paleocene–Eocene transition (see Fig. 6; Table 1). The glauconitization of preexisting particles (pellets and coprolites) was also suggested by many authors (e.g., Chabou-Mostefai, 1987; Kechiched et al., 2018; Laouar et al., 2024).

Petrographic analysis shows that glauconitization is more pronounced in the rim than the core of the pellet and coprolite particles, and therefore postdates the phosphatization processes (Laouar et al., 2024).

The shift in the main peak of glauconite to ~9.04 Å (±) (see Fig. 6) appears linked to the potassium content, which is the main interlayer cation. As illustrated in Odin and Fullagar (1988), Cretaceous-Paleogene glauconites exhibit variations in the 001 effect around 10 Å related to the potassium content. However, while these samples reach up to 4.8 % K_2O, the studied fine fraction does not exceed 1.79 % (K_2O: min = 0.32 wt%; max = 1.79 wt%; average = 0.75 ± 0.34 wt%). Velde (2014) noted a correlation between potassium content and glauconite mineral structure and this may explain the observed shift in the main peak of glauconite in our samples.

The low K_2O and Fe_2O_3 contents in both fine fractions (< 45 μm) and whole-rock samples (Kechiched et al., 2018) raise several questions about the origin and evolution of the glauconite particles. Based on the genetic classification of Odin and Matter (1981), which is in agreement with the low content of K_2O (<4 %) of both fine fraction and whole-rock (e.g., Kechiched et al., 2018; Laouar et al., 2024), these glauconitized grains are in fact immature glauconites. The observed greenish, rounded to sub-rounded glauconite grains, of a diameter ranging from 150 to 250 μm, are similar in shape to other phosphate particles, such as the pellets and coprolites (e.g., Ferhaoui et al., 2022). According to the "verdissement theory" of Odin and Matter (1981), the formation of mature glauconites requires semi-confined micro-environment within pores; this micro-environment is distinct from the surrounding seawater and needs wide pores, exceeding 400 μm, to facilitate the chemical reactions. The lack of these specific conditions is most likely the main reason for non-maturity of the glauconite minerals in the studied phosphorites.

5.2. REE distribution and fractionation processes

5.2.1. PAAS-normalized REY patterns

PAAS (Taylor and McLennan, 1985)-normalized REE + Y patterns offer crucial tools to decipher the paleoenvironmental conditions for phosphorite depositional processes. (e.g., Wright et al., 1984; Shields and Stille, 2001; Gnandi and Tobschall, 2003; Fazio et al., 2007; Garnit et al., 2012, 2017; Khan et al., 2016; Kocsis et al., 2016; Tostevin et al., 2016; Auer et al., 2017). In addition, previous study of Ferhaoui et al. (2022) has shown that REY geochemical signatures are similar in the grain size fractions from the same hosting samples indicating synchronized evolution of all rock components, therefore we have used REE-geochemistry to reconstruct paleo-environment conditions for the present study.

The PAAS-normalized REY patterns for the northern and southern basins are displayed in Fig. 9A-D and compared to various typical REE-patterns (Fig. 9E). The northern basin Djebel El Kouif and Djebel Dyr phosphorite patterns are relatively different compared to those from Kef Essenoun southern basin profiles. The northern deposits, except the lower beds from the Djebel El Kouif, show typical modern seawater with LREE depletion and HREE enrichment, along with a pronounced negative Ce and positive Y anomalies. As depicted from Fig. 9, a slight variation is observed from the lower to the upper beds, particularly, in the Kef Essenoun deposit in the south (Profil 2, Fig. 9 D). The Ce anomalies are well pronounced in upper beds relative to those of the main sub-layer in agreement with the evolution of the depositional conditions from sub-oxic to more oxic conditions; this is also evidenced by many authors when studying other phosphorite basins in North Africa (e.g., Garnit et al., 2017; Kechiched et al., 2020, 2024; Diab et al., 2024). These authors emphasize the more oxic conditions, open and shallow environments towards northern basins (e.g., Diab et al., 2024), and more restricted, sub-reduced conditions and deeper environments towards southern deposits (e.g., Kocsis et al., 2013; Laouar et al., 2024). The latter show relative enrichment of MREE (one-way Anova: $p < 0.01$) compared to HREE and LREE, together with higher amounts of REEs especially for glauconite-rich samples in both profiles, indicating additional control of REE by the glauconitization processes, particularly for MREE. Note that the slow sedimentation rate depicted from the Ce anomaly vs. Nd plot (Fig. 10A) enabled ion exchange from pore water that promotes glauconitization of the preexisting particles, but this was not enough to produce mature glauconite crystals, as mentioned by Laouar et al. (2024).

Table 3
Whole-rock major, trace and rare earth element contents of phosphorite matrix from the southern basin phosphorites.

Samples	KFS1	KFS2	KFS3	KFS4	KFS5	KFS6	KFS7–8	KS*1	KS*2	KS*3	KS*4	KS*5	KS*6	KS*7
Locality	Kef Essenoun (Profile 1)							Kef Essenoun (Profile 2)						
Major elements (wt%)														
SiO_2	16.3	18.64	14.83	19.85	16.93	14.01	10.49	37.39	38.98	24.13	27.88	23.58	17.9	13.28
Al_2O_3	3.21	3.56	2.76	3.74	4	3.31	2.2	6.96	7.43	5.03	5.32	6.65	4.8	2.91
Fe_2O_3(T)	1.42	1.39	1.1	0.91	0.71	0.7	0.43	2.85	2.34	1.96	2.41	2.25	1.65	1.32
MnO	0.03	0.013	0.008	0.009	0.007	0.005	< 0.005	0.023	0.014	0.009	0.014	0.012	0.009	0.006
MgO	5.11	2.66	5.28	4.71	7.19	2.57	1.64	8.58	2.77	3.14	2.17	4.02	4.26	5.26
CaO	34.23	34.61	35.18	31.03	31.17	37.49	38.73	13.69	16.46	30.26	28.53	28.16	32.55	36.61
Na_2O	1.19	1.4	1.07	1.22	0.93	1.63	2.17	0.16	0.49	0.59	0.74	0.81	0.77	0.78
K_2O	0.57	0.65	0.55	0.69	1.08	0.9	0.6	0.65	0.94	0.72	0.9	1.28	1.79	0.98
TiO_2	0.082	0.086	0.084	0.088	0.073	0.058	0.051	0.305	0.313	0.143	0.111	0.188	0.152	0.122
P_2O_5	17.22	19.86	17.48	15.36	12.82	21.33	22.24	0.9	6.7	10.15	16.03	14.21	16.52	17.37
Cu/Al_2O_3	6.231	5.618	3.623	2.674	2.500	3.021	13.636	2.874	6.729	3.976	3.759	3.008	4.167	6.873
Trace elements (ppm)														
Sc	4	4	4	4	3	3	3	7	7	5	4	5	3	2
Be	2	2	2	2	2	2	1	2	2	2	2	3	2	1
V	196	169	108	140	183	169	502	96	687	157	184	214	241	155
Ba	40	35	24	41	44	43	70	42	49	35	57	80	47	43
Sr	1523	1680	1419	1615	1498	2010	1779	212	575	1097	1771	1367	1075	1089
Y	155	187	187	149	109	157	128	9	45	113	185	165	95	61
Zr	34	39	34	35	28	29	26	60	74	62	60	70	53	41
Cr	610	680	500	590	540	510	710	170	810	1040	1000	1220	560	370
Co	10	10	< 1	2	< 1	3	< 1	3	3	< 1	3	2	< 1	< 1
Ni	90	50	30	30	20	30	50	30	150	70	110	80	90	70
Cu	20	20	10	10	10	10	30	20	50	20	20	20	20	20
Zn	270	230	200	150	90	120	660	110	440	550	530	590	390	330
Ga	5	5	5	4	3	3	4	9	10	8	6	9	6	5
Ge	< 1	< 1	< 1	< 1	< 1	< 1	1	< 1	< 1	1	2	2	1	< 1
As	15	9	5	< 5	< 5	< 5	< 5	< 5	< 5	11	20	9	8	8
Rb	10	12	10	11	11	9	7	28	28	16	16	21	21	17
Nb	3	3	3	4	2	2	2	7	7	4	3	6	6	5
Mo	4	4	3	4	3	3	5	5	31	42	48	16	36	35
Ag	4.7	4.2	2.4	1.2	0.5	0.7	1.3	< 0.5	2.9	6.2	9.4	3.9	3.8	1.8
In	< 0.2	< 0.2	< 0.2	< 0.2	< 0.2	< 0.2	< 0.2	< 0.2	< 0.2	< 0.2	< 0.2	< 0.2	< 0.2	< 0.2
Sn	1	1	< 1	< 1	< 1	< 1	< 1	2	2	1	1	1	1	1
Sb	1.4	1.1	0.8	0.7	< 0.5	0.6	0.6	< 0.5	< 0.5	1.5	2.9	1.4	1.7	1.1
Cs	0.5	0.6	0.6	0.6	0.5	< 0.5	< 0.5	2.1	2	1.1	0.8	1.3	1.1	1
Hf	0.8	0.9	0.8	0.8	0.7	0.7	0.6	1.3	1.2	1.2	1.3	1.5	1.1	0.8
Ta	0.3	0.3	0.3	0.3	0.2	0.3	0.3	0.5	0.5	0.4	0.4	0.5	0.5	0.4
W	7	5	< 1	5	< 1	6	6	< 1	< 1	< 1	< 1	< 1	< 1	< 1
Tl	13.4	11.6	4.5	5.7	2.9	2.2	1.9	0.2	2.2	3.4	21.8	14.9	5.9	4.9
Pb	6	7	< 5	6	< 5	5	5	< 5	< 5	5	7	6	< 5	< 5
Bi	< 0.4	< 0.4	< 0.4	< 0.4	< 0.4	< 0.4	< 0.4	< 0.4	< 0.4	< 0.4	< 0.4	< 0.4	< 0.4	< 0.4
Th	13.3	18.4	19.4	14.8	10.7	13.5	4.7	3.9	4.6	15.1	23.3	21.4	9.2	4.9
U	39.1	38.6	34	31.4	24.7	36.9	54.3	3.2	42.3	22.4	31.7	27.1	44.6	33.4
Rare earth elements (ppm)														
La	113	141	140	114	81.5	122	71	16.9	36.7	87.6	147	130	75.4	49
Ce	152	205	205	164	116	172	58.1	26.6	42.6	134	222	198	105	62.7
Pr	25.6	33.3	32.7	26.3	19.1	27.4	12.6	3.1	6.23	20.9	35.3	30.9	16.1	9.86
Nd	107	140	138	109	79.1	115	53.1	12.1	25.9	87.5	150	130	66.7	39.7
Sm	21.6	28.3	28.7	22.3	16.3	23.2	10.6	2.4	5.4	18.2	30.4	26.9	13.1	7.7
Eu	5.02	6.55	6.44	5.11	3.74	5.3	2.65	0.56	1.3	4.31	7.09	6.14	3.16	1.93
Gd	20.6	26.6	26.7	21.8	15.4	22	12.4	2	5.1	17	28	25	12.6	7.7
Tb	3	3.8	3.9	3	2.2	3	1.9	0.3	0.8	2.5	4	3.6	1.8	1.2
Dy	17.8	22.4	22.3	17.7	12.5	18.4	12.2	1.8	4.8	14.2	22.9	20.5	10.8	6.8
Ho	3.6	4.7	4.6	3.6	2.6	3.8	2.7	0.3	1	2.9	4.6	4	2.3	1.4
Er	10.4	12.8	12.5	10.3	7.4	10.7	8.1	0.9	3	8.1	12.8	11.5	6.4	4.1
Tm	1.38	1.7	1.7	1.37	0.98	1.42	1.1	0.14	0.43	1.07	1.73	1.53	0.83	0.56
Yb	8.3	10.2	10.2	8.3	6	8.6	6.9	0.9	2.6	6.3	10.3	9.1	5	3.4
Lu	1.37	1.58	1.6	1.28	0.95	1.32	1.18	0.14	0.42	0.97	1.63	1.45	0.8	0.51
REEs	490.67	637.93	634.34	508.06	363.77	534.14	254.53	68.14	136.28	405.55	677.75	598.62	319.99	196.56
REY	645.67	824.93	821.34	657.06	472.77	691.14	382.53	77.14	181.28	518.55	862.75	763.62	414.99	257.56
LREE (La—Nd)	397.6	519.3	515.7	413.3	295.7	436.4	194.8	58.7	111.43	330	554.3	488.9	263.2	161.26
MREE (Sm—Dy)	68.02	87.65	88.04	69.91	50.14	71.9	39.75	7.06	17.4	56.21	92.39	82.14	41.46	25.33
HREE (Ho—Lu)	25.05	30.98	30.6	24.85	17.93	25.84	19.98	2.38	7.45	19.34	31.06	27.58	15.33	9.97
(La/Nd)N	0.937	0.894	0.900	0.928	0.914	0.941	1.187	1.239	1.257	0.888	0.870	0.887	1.003	1.095
(Sm/Yb)N	1.322	1.410	1.430	1.365	1.380	1.371	0.781	1.355	1.055	1.468	1.500	1.502	1.331	1.151

(*continued on next page*)

Table 3 (*continued*)

Samples	KFS1	KFS2	KFS3	KFS4	KFS5	KFS6	KFS7–8	KS*1	KS*2	KS*3	KS*4	KS*5	KS*6	KS*7
Locality	Kef Essenoun (Profile 1)							Kef Essenoun (Profile 2)						
(Sm/Pr)N	1.342	1.352	1.396	1.349	1.358	1.347	1.338	1.232	1.379	1.385	1.370	1.385	1.295	1.242
(La/Sm)N	0.760	0.724	0.709	0.743	0.726	0.764	0.973	1.023	0.987	0.699	0.703	0.702	0.836	0.925
(La/Yb)N	1.005	1.020	1.013	1.014	1.003	1.047	0.760	1.386	1.042	1.026	1.054	1.055	1.113	1.064
(Gd/Yb)N	1.502	1.578	1.584	1.589	1.553	1.548	1.088	1.345	1.187	1.633	1.645	1.663	1.525	1.370
Eu/Eu*	1.121	1.124	1.095	1.091	1.112	1.105	1.088	1.204	1.166	1.154	1.144	1.115	1.158	1.180
Pr/Pr*	1.145	1.125	1.114	1.129	1.141	1.118	1.243	1.016	1.086	1.110	1.108	1.107	1.110	1.140
Ce/Ce*	0.631	0.671	0.678	0.673	0.662	0.663	0.414	0.807	0.598	0.705	0.690	0.701	0.669	0.632
Ce anomaly	−0.200	−0.173	−0.169	−0.172	−0.179	−0.179	−0.383	−0.093	−0.223	−0.152	−0.161	−0.154	−0.175	−0.199
Y/Y*	1.544	1.454	1.473	1.489	1.525	1.497	1.778	0.970	1.638	1.404	1.437	1.452	1.520	1.577
Y/Ho	43.056	39.787	40.652	41.389	41.923	41.316	47.407	30.000	45.000	38.966	40.217	41.250	41.304	43.571

5.2.2. REE and paleo-redox conditions

In oxic conditions, Cerium Ce^{3+} may be oxidized into Ce^{4+}; thus, the REE patterns in oxygenated modern marine environments exhibit a strong negative Ce anomaly (De Baar et al., 1988; German et al., 1991; Bau et al., 1997; Bau, 1999; De Carlo and Green, 2002). Therefore, the sediments that were deposited in such environments would display also a negative Ce anomaly (e.g., Koeppenkastrop and De Carlo, 1992). Therefore, Ce anomaly may be used to decipher the redox conditions of the depositional environment (Alibo and Nozaki, 1999; Morad and Felitsyn, 2001; Haley et al., 2004; Garnit et al., 2012). Post-depositional conditions, particularly diagenesis and reworking, may also influence the Ce anomaly, modifying the original signatures (Abedini and Asghar Calagari, 2017; Auer et al., 2017). In addition, the $(La/Yb)_N$, $(La/Sm)_N$ and Pr/Pr* ratios can be of use to check Ce anomaly significance (Bau and Dulski, 1996; Reynard et al., 1999). It is also known that negative Ce anomalies associated with values of $(La/Sm)_N < 0.35$ should not be used to depict redox conditions, because middle REE (MREE) enrichment during early diagenesis implies incorporation of significant Nd, Sm, Eu, Gd, and Tb amounts relative to La and Ce (Reynard et al., 1999; Morad and Felitsyn, 2001; Salama et al., 2018). Fine-grained matrix samples from this study yield $(La/Sm)_N > 0.35$ (See Tables 2 and 3) and, hence, can be used to check the reliability of Ce anomaly.

Further, $(La/Yb)_N$ and $(La/Sm)_N$ ratios in this study exhibit similar values to those reported for the whole-rock by Kechiched et al. (2020), ranging from 0.58 to 1.38, and from 0.7 to 1.33, respectively. While $(La/Sm)_N$ ratios in these samples remain unchanged and align with the range proposed for modern seawater, $(La/Yb)_N$ ratios in the fine fraction samples from the two sites are slightly higher than those reported for modern seawater by Reynard et al. (1999), implying adsorption of light REE (Reynard et al., 1999; Fazio et al., 2007; Kechiched et al., 2020). The $(La/Yb)_N$ and $(La/Sm)_N$ ratios of the studied samples are represented on the $(La/Yb)_N$ versus $(La/Sm)_N$ diagram proposed by Reynard et al. (1999); those of the northern basin plot closer to the field of modern seawater, compared to those of southern basin (Fig. 10B). According to this distribution, it is suggested that REE uptake through adsorption processes occur at the water/sediment interface during early diagenesis and remained unchanged during late diagenesis. This indicates minor changes over time (Mongelli et al., 2018).

It is also well known that high La concentrations may affect the estimation of Ce values. For this, Bau and Dulski (1996) proposed the Pr/Pr* versus Ce/Ce* diagram (Fig. 10C) to better evaluate the Ce anomalies. On this diagram, all the studied samples plot in field IIIb, where the samples from the Djebel El Kouif and Djebel Dyr of the northern basin exhibit more oxic conditions, compared to those from Kef Essenoun phosphorites in the southern basin. Also, within the Kef Essenoun deposit, samples from the basal sub-layer show more reducing conditions than those of the main sub-layer, which indicates an evolution from reduced to sub-oxic conditions with time.

Europium can be also affected by changes in the redox conditions. This element can be reduced to divalent (Eu^{2+}) from its initial trivalent state (Eu^{3+}) under reduced conditions (e.g. Brookins, 1989; Shields and Stille, 2001). Therefore, this element also serves as a useful tool to assess the depositional conditions, displaying positive anomaly under reduced to anoxic conditions, high temperatures, and hydrothermal REE supply (Michard et al., 1983; Stalder and Rozendaal, 2004; Schmidt et al., 2007; Bau et al., 2010). The reduction from Eu^{3+} to Eu^{2+} requires an oxidation potential lower than −0.43 V, with a minimum pH of 3.7 (Garrles and Christ, 1965). The samples from phosphorites of the northern basin exhibit Eu/Eu* ratios ranging from 0.99 to 1.18 with an average of 1.09 ± 0.07, whereas, those from Kef Essenoun of southern basin display slightly higher Eu/Eu* ratios ranging from 1.09 to 1.2 (average = 1.13 ± 0.04). This reflects sub-oxic to sub-reduced conditions to the south and oxic conditions in northern Basin.

5.2.3. REE and siliciclastic input, and diagenesis

Yttrium is often considered as an element that belongs to the rare earth element group, where it is frequently placed between (Dy) and (Ho) based on its atomic number, ionic radius and similar behavior to that of Ho (e.g., Zhang et al., 1994; Bau, 1996; Bau and Dulski, 1996). Yttrium anomaly and the $(La/Nd)_N$ ratio typically exhibit positive values in seawater. However, the magnitude of these patterns can be reduced by diagenetic processes (Zhang et al., 1994; Bau, 1996; Shields and Stille, 2001; Fazio et al., 2007). Nevertheless, these two parameters can serve as indicators of post-depositional changes during fluid circulation (Fazio et al., 2007). Plotted samples on the Y anomaly versus $(La/Nd)_N$ diagram of Shields and Stille (2001) show that most of them fall within the seawater field shown on Fig. 10D. From this figure, it can also be seen that samples from the northern basin phosphorites, with the Y/Y* ratios ranging from 1.55 to 2.37 (average = 1.85 ± 0.28), tend to be slightly affected by the weathering process. On the other hand, the majority of samples from Kef Essenoun, with Y anomaly varying between 0.97 and 1.78 (average = 1.48 ± 0.18) are rather influenced by early diagenesis, especially those of the main sub-layer.

Furthermore, the Y/Ho ratio is a valuable proxy for understanding the influence of detrital siliciclastic input. Differences in speciation lead to various behaviors during scavenging, a process controlling the REY distribution in seawater (e.g., Byrne and Kim, 1990; Bau and Dulski, 1994). In marine conditions, the fractionation between Y and Ho primarily arises from their different reactivities, where Ho typically tends to be more scavenged by hydrogenous ferromanganese oxyhydroxide particles than Y (Bau, 1996, 1999; Koschinsky et al., 1997). For modern seawater, Bau and Dulski (1994) reported a range of Y/Ho ratios between 47 and 77. In the northern basin, Y/Ho ratios in the samples from Djebel El Kouif range from 46 to 61, fitting well within the range of seawater values reported by Bau and Dulski (1994), whereas, two samples from Djebel Dyr exhibit slightly lower ratios (40 and 42; Table. 2). This eliminates the possibility of a significant impact of terrigenous inputs in the northern basin. On the other hand, all phosphorite samples from the Kef Essenoun deposit in the southern basin fall well below the seawater range, displaying Y/Ho ratios ranging from 30 to 47, with an average of 41.13 ± 3.89. The lowest values being recorded in the basal sub-layer. In addition, $(Sm/Yb)_N$ ratios display high values in the southern basin, with an enrichment of MREE, indicating hydrogenous ferromanganese oxyhydroxide control, also alluded by Tahar-Belkacem

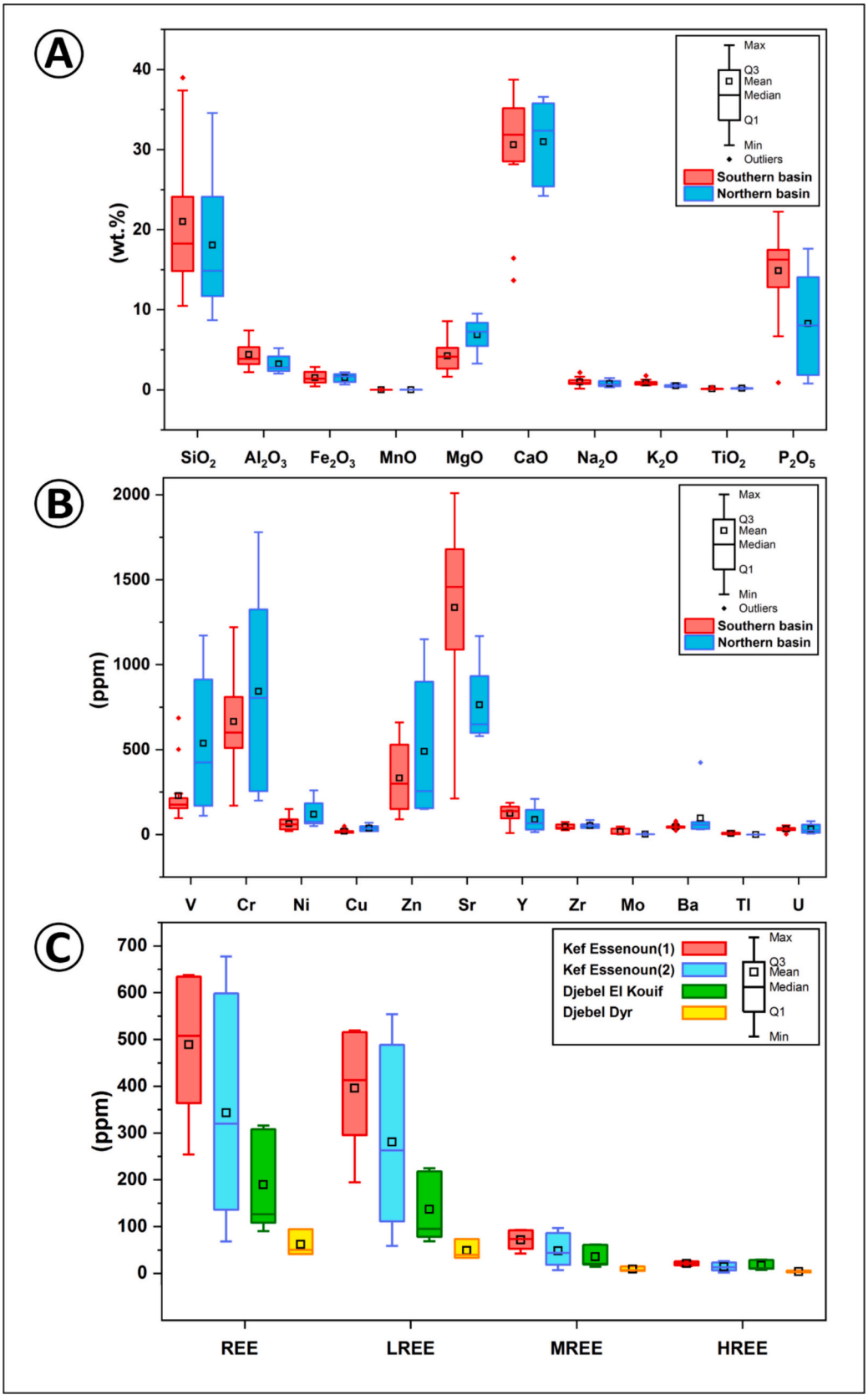

Fig. 7. Box and whiskers plots of major (A), trace (B) and rare earth elements (C) of the investigated samples.

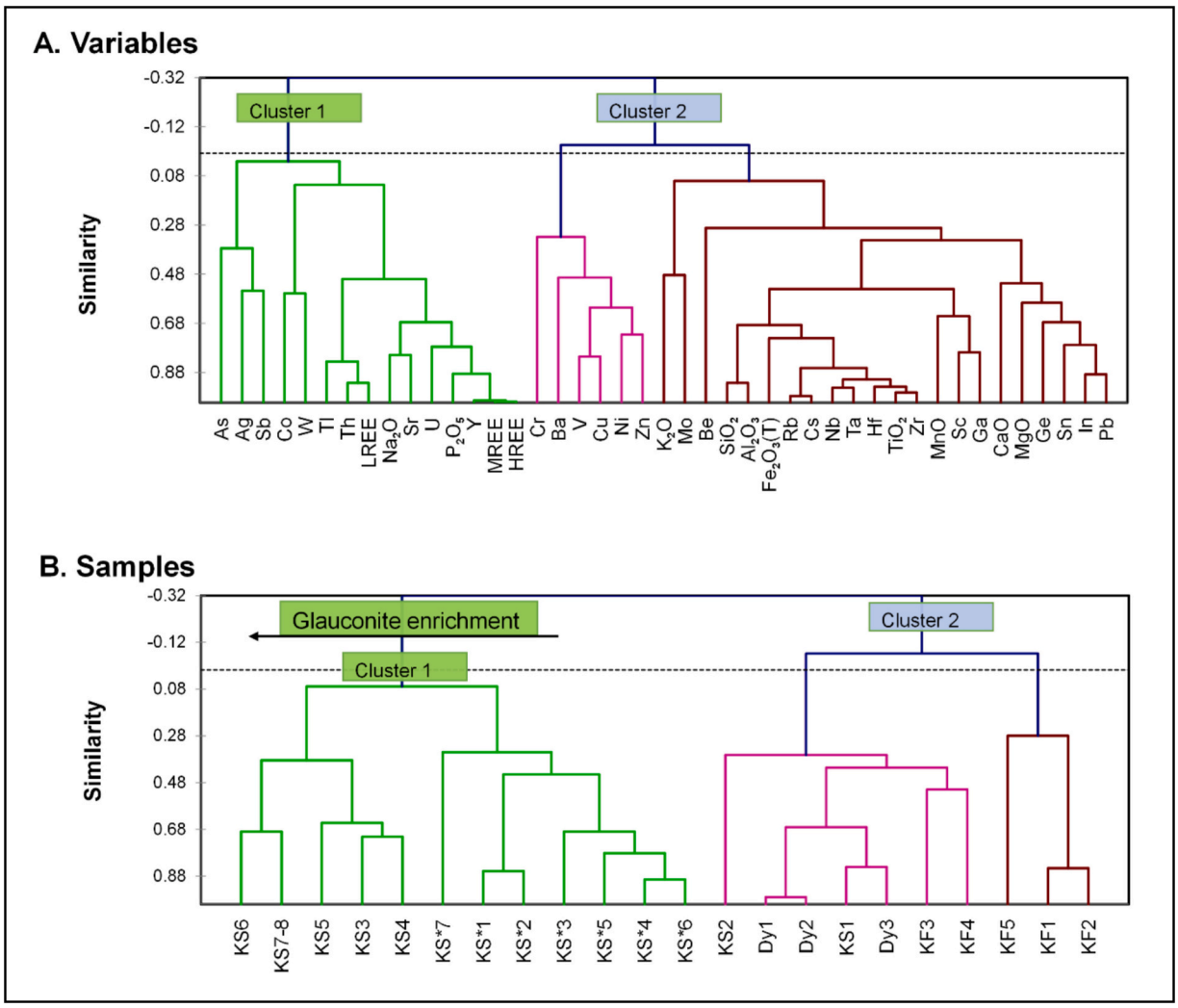

Fig. 8. Hierarchical cluster analysis dendrograms of (A) clr-variables and (B) samples clustering.

et al. (2024) (Fig. 10E-F). This may be due to the high MREE contents in the most glauconitized samples (Tables. 2 and 3), which are logically Fe-enriched.

5.3. *Paleoclimate and paleoenvironment versus glauconitization*

The Paleogene was interrupted by multiple global warming events, most notably the Paleocene–Eocene Thermal Maximum (PETM), ETM2 (or ELMO), and ETM3, alongside several transient climatic perturbations (Zachos et al., 2001; Cramer et al., 2003; Lourens et al., 2005; Nicolo et al., 2007; Stap et al., 2010). These events were marked by abrupt temperature rises, pronounced carbon isotope excursions, and major paleoenvironmental changes (Zachos et al., 2001). Their origins remain debated, with hypotheses ranging from magmatic intrusions to the destabilization of methane hydrates or permafrost (Dickens et al., 1995; Svensen et al., 2004, 2010; Westerhold et al., 2009; De Conto et al., 2012; McInerney and Wing, 2011). Although regional volcanism remains a plausible driver, it lacks conclusive evidence.

This interval also witnessed a remarkable increase in authigenic mineral formation, particularly glauconite, within marine sediments along the southern paleo-Tethyan margin, including North Africa, Southern Europe, the Middle East, and India (Banerjee et al., 2020). Within this Paleogene glauconites, 49 % occurrences were formed during the Eocene, 35 % during the Paleocene, and 16 % during the Oligocene (Banerjee et al., 2016a). Glauconite-phosphorite associations, identified in 17 cases and including Kef Essenoun and Djebel El Kouif, are consistently linked to warm climatic intervals (Banerjee et al., 2019, 2020; Kechiched et al., 2018, 2020; Buccione et al., 2021).

Warm and humid conditions likely enhanced continental weathering, enriching oceanic nutrient supplies, boosting organic productivity, and altering redox conditions, factors conducive to glauconitization, especially within semi-restricted environments characterized by low sedimentation rates (Odin and Matter, 1981; Van Houten and Purucker, 1984; Alessandro Amorosi, 1995; El Albani et al., 2005; Peters and Gaines, 2012; Banerjee et al., 2016b; Baldermann et al., 2017; Bansal et al., 2020; Roy Choudhury et al., 2021). Glauconite formation was further controlled by substrate properties and seawater temperature (Odin and Fullagar, 1988; Bansal et al., 2019; Banerjee et al., 2020).

XRD analyses by Kechiched et al. (2020) revealed Heulandite (d-spacing = 8.96 Å) in whole-rock samples from both sites. This mineral typically forms through the alteration of acidic volcanic materials or as a cavity filling in basaltic rocks (Merkle and Slaughter, 1968). Hence, its presence, along clinoptilolite, and feldspar, ilmenite and zircon may signal probable volcanism as also suggested for nearby Tunisian basins (e.g., Clocchiatti and Sassi, 1972; Galfati et al., 2010; Garnit et al., 2017).

Within this scenario, some elemental ratios, such as the Cu/Al one, may further constrain basinal productivity. Cu/Al values range from 3.99 to 26.55 (avg. 13.11 ± 8.31) in the northern basin, suggesting higher productivity, whereas southern values range from 2.5 to 13.64

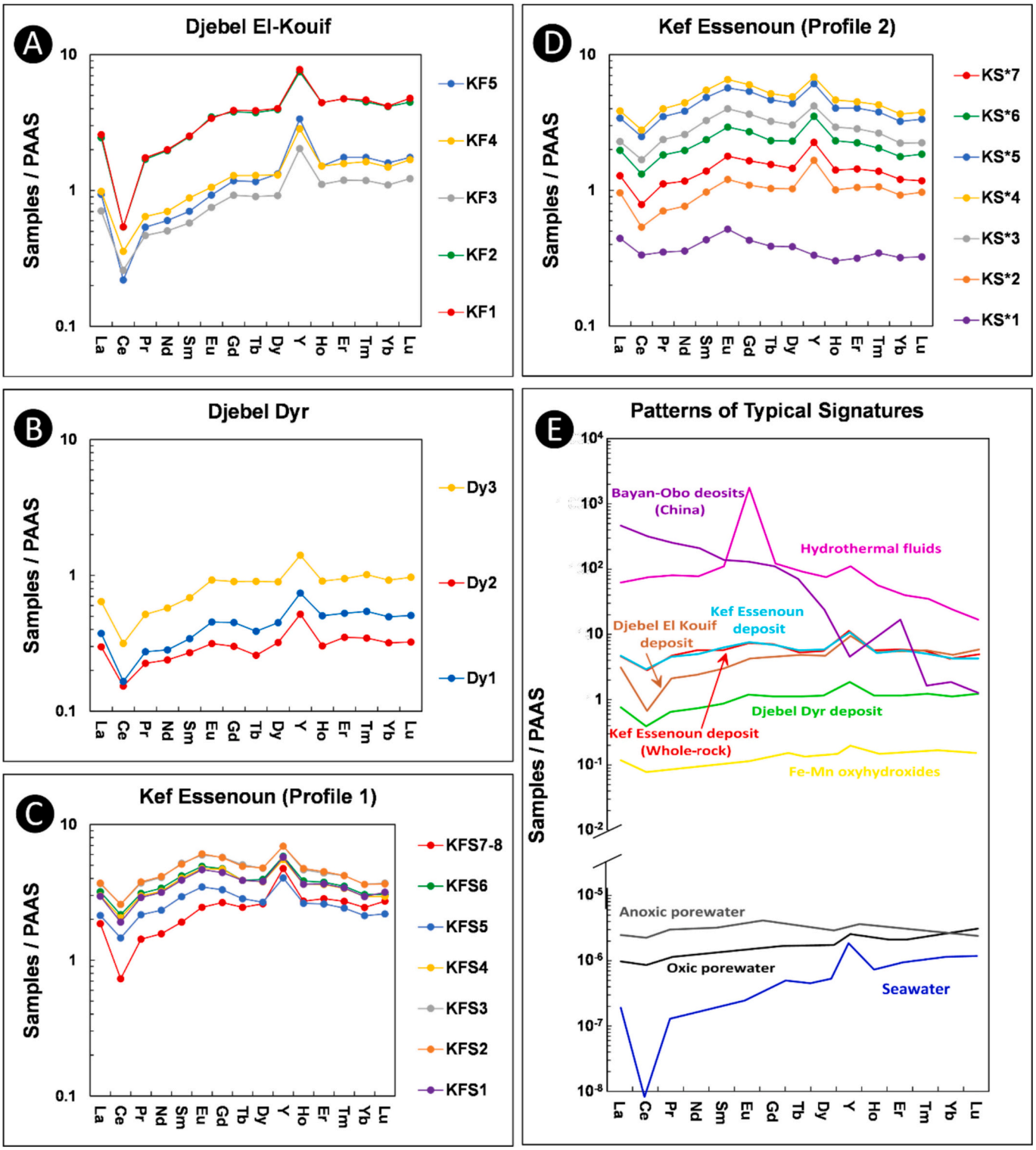

Fig. 9. (A, B, C, D) PAAS normalized (McLennan, 1989) REE + Y patterns of investigated samples. (E) PAAS-Normalized (McLennan, 1989) REE+Y Patterns of several typical signatures from the literature: Djebel El Kouif deposit, Djebel Dyr deposit, Kef Essnoun deposit (This study); Kef Essenoun deposit (Whole-rock) (Kechiched et al., 2020); Bayan-Obo deposits (Zhang et al., 2017); Hydrothermal fluids (Bau and Dulski, 1999); Oxic and anoxic marine porewaters (Haley et al., 2004; Abbott et al., 2015); Fe—Mn oxyhydroxides (Palmer and Elderfield, 1986; Bayon et al., 2004; Charbonnier et al., 2012); Seawater (De Baar et al., 1985; Shimizu et al., 1994; Alibo and Nozaki, 1999; Garcia-Solsona et al., 2014; Osborne et al., 2015).

(avg. 4.91 ± 2.94), reflecting lower to moderate productivity. The Ce/Ce* ratio ranges from 0.23 to 0.55 in the north and from 0.41 to 0.81 in the south. Lower Ce/Ce* values in the north indicate more oxic conditions, which appear contradictory given the high productivity. This discrepancy could be attributed to enhanced seawater circulation in the northern basin, ensuring a continuous influx of oxygenated waters and stabilizing redox conditions despite elevated organic matter input. Additionally, higher Al contents in the southern basin associated with clay-rich facies, may result in lower Cu/Al ratios. Therefore, these ratios must be interpreted cautiously, particularly under extreme climatic

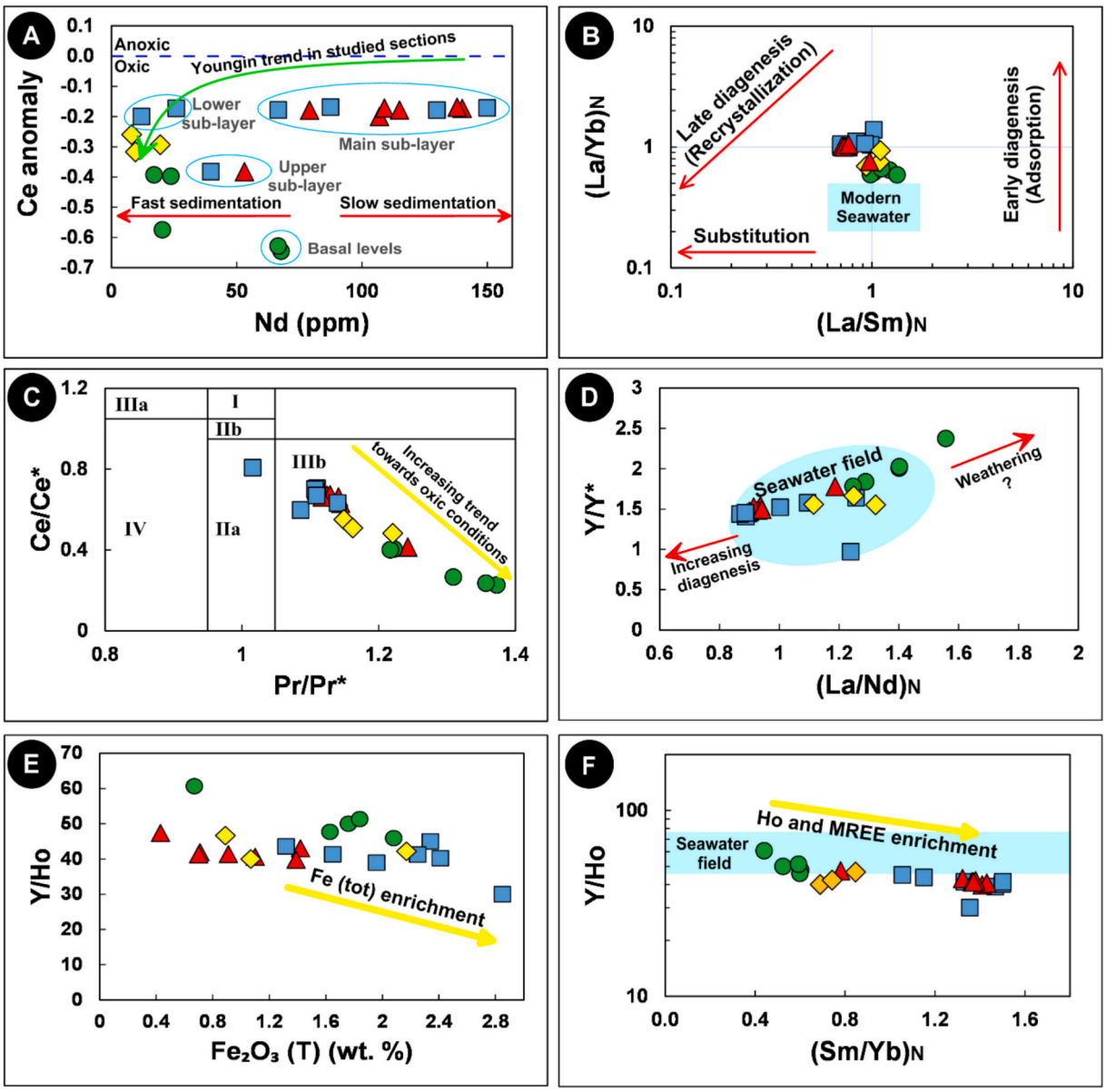

Fig. 10. REE binary diagrams showing the evolution of the depositional conditions. (A) Ce anomaly vs Nd (after Wright et al., 1987). (B) $(La/Yb)_N$ vs $(La/Sm)_N$ (after Reynard et al., 1999). (C) Ce/Ce* vs Pr/Pr* (after Bau and Dulski, 1996). (D) Y/Y* vs $(La/Nd)_N$ (after Shields and Stille, 2001). (E) Y/Ho vs Fe_2O_3 (after Kechiched et al., 2020). (F) Y/Ho vs $(Sm/Yb)_N$ (seawater range after Bau and Dulski, 1994).

conditions. Notably, Ce depletion in seawater is influenced by factors beyond redox potential, including microbial activity, pH, depth, and seawater age (Brookins, 1989; German and Elderfield, 1990; Moffett, 1990; Piepgras and Jacobsen, 1992; Tricca et al., 1999).

Based on the previously referenced literature and relying on the results obtained in this study, we propose un updated summary in Fig. 11, for the formation of immature glauconitic particles in the study area. During the late Paleocene–early Eocene, intensified weathering delivered abundant nutrients to the ocean, enhancing primary productivity and reducing surface-water oxygen levels. In the semi-restricted southern basin, diminished upwelling and slow sedimentation rates allowed prolonged exposure of fecal pellet substrates to seawater, favoring glauconitization. Ion exchange between porous substrates and ambient waters further promoted mineral authigenesis. The higher glauconite content observed in the south compared to the north may reflect more favorable conditions, shaped by basin morphology (restricted south, open north), terrigenous input, and paleoclimate. Thus, glauconitization during the Paleogene resulted from the interplay of climatic, geochemical, and depositional controls.

Due to the brief duration of many warm events, precise chronological resolution remains challenging. Nonetheless, the southern margin of the Tethys represents a key archive for decoding paleoenvironmental responses to global warming during the Paleogene.

5.4. Economic evaluation of REE outlook

5.4.1. REE enrichment and outlook coefficient (C_{outl})

Following their vital applications in high-tech, green economy, pharmaceutical and industrial sectors, the REE demand is continuously increasing; thus, posing significant economic challenges to cover the global needs for these elements. According to the U.S. Geological Survey (2024), the global production of rare earth oxides (REO) is projected to

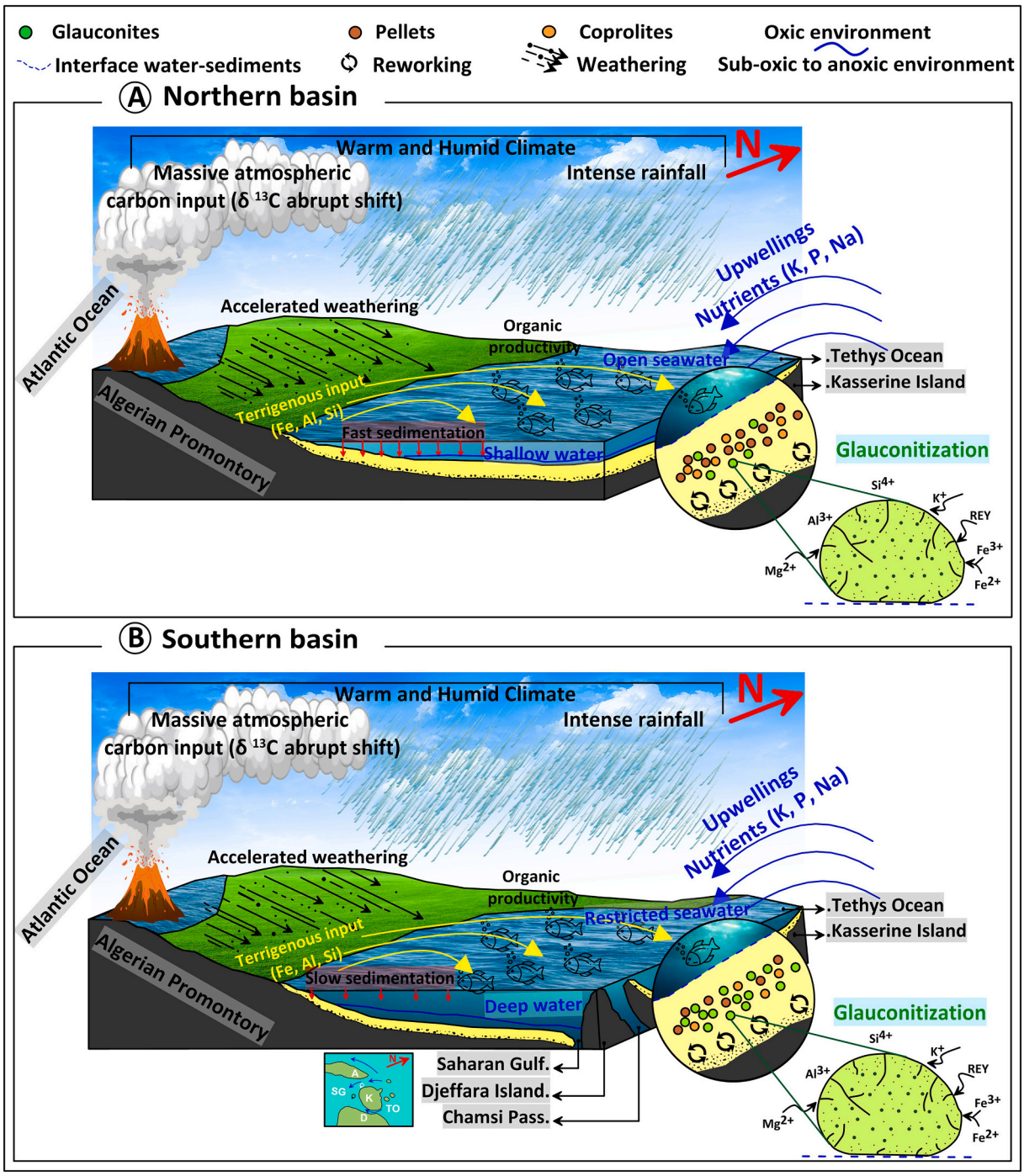

Fig. 11. A simplified model summarizing the geological history of glauconitization process within the Algerian phosphorites: (A) Northern Basin, (B) Southern Basin. Upadted from the Kechiched et al. (2018) and based on the following literature, combined with interpretations from this study: Basin configuration (Kocsis et al., 2013; Kechiched et al., 2018; this study), Paleogeography (Sassi, 1974; Burollet and Oudin, 1980; Winnock, 1980; Chaabani, 1995; Zaïer et al., 1998), REE signatures and redox environments (Kechiched et al., 2020; Diab et al., 2024; Laouar et al., 2024; this study), Paleoclimate (Clocchiatti and Sassi, 1972; Zachos et al., 2001, 2005; Svensen et al., 2004, 2010; Westerhold et al., 2009; Galfati et al., 2010; McInerney and Wing, 2011; Garnit et al., 2017; Banerjee et al., 2020), Glauconitization process and conditions (Odin and Matter, 1981; Van Houten and Purucker, 1984; Alessandro Amorosi, 1995; El Albani et al., 2005; Peters and Gaines, 2012; Banerjee et al., 2016b; Baldermann et al., 2017; Bansal et al., 2020; Roy Choudhury et al., 2021), Sedimentological processes (Kechiched et al., 2018, 2020, 2024; this study).

reach 350,000 metric tons, reflecting an increase of 50,000 metric tons compared to 2022. Nevertheless, the global reserves of rare earth elements (REEs) are estimated to be 110 million metric tons in 2023 (U.S. Geological Survey, 2024). Due to its significant REE-rich carbonatite deposits, China dominates the global production of rare earth elements (Xu et al., 2008; Xie et al., 2015; Ni et al., 2020). According to the European Commission (Grohol and Veeh, 2023), China is the largest global supplier of REEs, providing 95 % of the total REEs, with: 85 % of ∑LREEs, 98 % of ∑MREEs, and 100 % of ∑HREEs.

Several alternatives can serve as secondary REE sources, including coal, bauxite, and phosphorites (Seredin and Dai, 2012; Buccione et al., 2021; Mongelli et al., 2021; Ji et al., 2022). Recycling batteries, magnets, and fluorescent lamps also provides limited REE recovery (U.S. Geological Survey, 2024). Among these, phosphorites have the highest

potential (e.g., Christmann, 2014; Emsbo et al., 2015; Wu et al., 2018; Peiravi et al., 2020; Ferhaoui et al., 2022). North Africa's Upper Cretaceous–Eocene phosphorite deposits hold over 54 billion metric tons of phosphorite rocks, representing 74 % of global reserves. Algerian phosphorites (576–906 ppm REEs) rank second after U.S. deposits (Buccione et al., 2021), with REY concentrations reaching 2572 ppm in glauconitic particles (Laouar et al., 2024).

Evaluating REE deposit profitability requires factors beyond REE + Y content, LREE/HREE ratios, and REE classification (Seredin, 2010). Industry demand and element criticality are essential. Based on these, Seredin (2010) classified REEs as critical (Nd, Tb, Dy, Y, Eu, Er), uncritical (La, Pr, Sm, Gd) and excessive (Ce, Ho, Tm, Yb, Lu). The outlook coefficient (C_{outl}) and the critical to excessive REY ratios (REY_{def}), indicate economic potential, with higher values favoring industrial demand. Ore classification ranges from ($REY_{def} \leq 26$ % and $C_{outl} \leq 0.7$), to promising ores (33 % $\leq REY_{def} \leq$ 50 %; $0.9 \leq C_{outl} \leq 3.1$), to highly promising ores ($REY_{def} \geq 62$ % and $C_{outl} \geq 2.8$) (Seredin and Dai, 2012). This approach could be updated according to the changes in the industry demand of individual REEs, along with the industry development of these elements (Seredin, 2010).

Plotting the studied samples from the northern and southern basin phosphorites of the Tebessa region on the C_{outl} vs. REY_{def} diagram, in comparison with global phosphorites and conventional REE ores (Fig. 12), reveals that the matrix spans from promising ores (33 % $\leq REY_{def} \leq$ 50 %; $0.9 \leq C_{outl} \leq 3.1$) to highly promising ores ($REY_{def} \geq 62$ % and $C_{outl} \geq 2.8$).

Nevertheless, it is worth mentioning that higher C_{outl} and REY_{def} values do not necessarily reflect the potential of a REE ore. For example, samples from the Carboniferous-Permian deposits in northern Alaska (Dumoulin et al., 2011) exhibit a C_{outl} reaching 10.7 (averaging 8.15) with a REY_{def} average of 62.11 %, which suggests promising ores. However, the average REE contents in these samples do not exceed 281.5 ppm, compared to the average REY contents of 512 ppm, with Y alone accounting 46.86 % of this value. Thus, it is evident that this discrepancy is mainly due to Y enrichment. A similar case is observed in the Moroccan phosphorites (data after Kocsis et al., 2016). These exhibit high C_{outl} and REY_{def}, where C_{outl} reaches 6.98 in some areas and averaging 4.47, with an average REY_{def} of 60.87 %. However, when examining the REE and REY contents, the data show that the average REY contents is 110.58 ppm, with 44.66 % of Y contribution, while the REE content averages only 62.44 ppm. Another example is that of the conventional REE ores of Bayan-Obo (China) (Zhang et al., 2017; Xiao-Zhi Hou et al., 2020). Despite it dominates the global REE production due to the very high REE content, reaching 45,000 ppm; the very low C_{outl} and REY_{def} reflect an unpromising ore. This is attributed mainly to the high LREE enrichment that makes up about 98 % of the total REE. In this regard, the C_{outl}, REY_{def}, REE and REY contents should be combined together with the ratios of LREE, MREE and HREE to the total REE contents, in order to get better insights.

The necessary minimum industrial grade for the extraction of REEs from a secondary source is generally estimated to be up to 300 ppm (Zhao et al., 2024). The high industrial recovery potential is estimated to correlate with ores showing a C_{outl} greater than 0.7, along with a REY_{def} exceeding 30 % (Zhao et al., 2024). The recent studies on the southern basin Djebel Onk phosphorites (Kef Essenoun: Buccione et al., 2021; Ferhaoui et al., 2022; Bled El Hedba: Laouar et al., 2024) indicate promising to highly promising REE extraction potential in Algerian phosphorites, based on the outlook coefficient (C_{outl}) and the percentage of critical REE.

Previous exploration studies were mainly focused on P_2O_5 contents of both whole-rock and particle separates that are used in fertilizer production, whereas the phosphorite matrix, often considered waste,

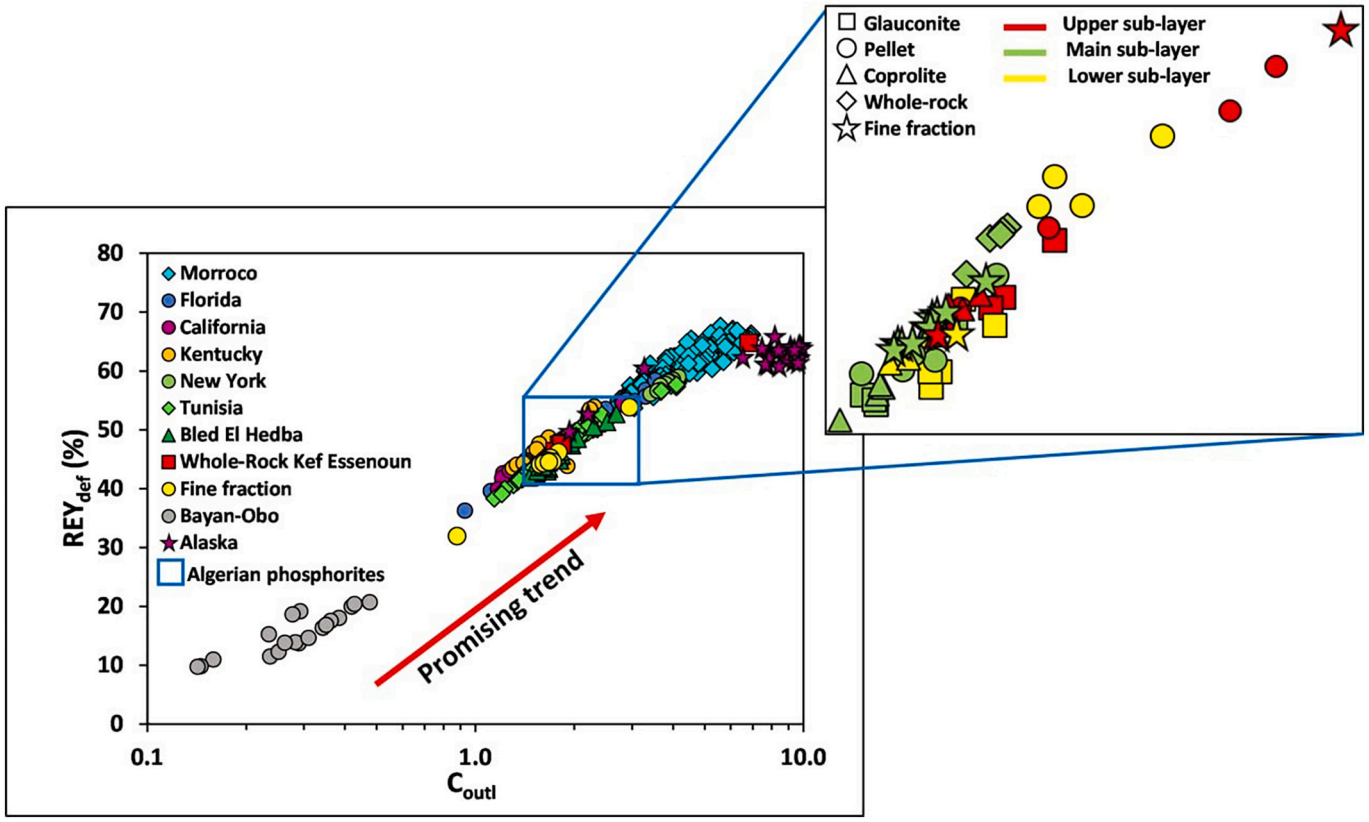

Fig. 12. Classification of REE-bearing phosphorite deposits based on the outlook coefficient (C_{outl}) versus the percentage of critical elements in the ΣREE (REY_{def}) (after Seredin, 2010). Data from: Tunisia (Ounis et al., 2008; Garnit et al., 2012, 2017); Morocco (Kocsis et al., 2016); Algeria (Kechiched et al., 2020; Laouar et al., 2024; This study); Florida, California, New York and Kentucky (Emsbo et al., 2015); Alaska (Dumoulin et al., 2011); Bayan-Obo (Zhang et al., 2017; Hou et al., 2020).

remains underexplored. The present study is also conducted to assess the economic potential of the phosphorite matrix of the phosphorites from the northern and southern basins of Tebessa region. For instance, the Kef Essenoun deposit in the south exhibits higher REE concentrations (up to 678 ppm) than those of the northern deposits (up to 316 ppm). These high REE contents, along with REY contents (up to 863 ppm), point to a real potential secondary REE source. Further, the highest REE concentrations occur within glauconite-rich phosphorite levels, where glauconite particles host the highest REE contents among the phosphatic particles. Given its iron content, glauconite may facilitate REE extraction and separation (Laouar et al., 2024).

Geochemical analysis conducted on the fine fraction (matrix) in this study, as well as on whole-rock samples (Kechiched et al., 2020) and mining wastes (Boumaza et al., 2021, 2024), reveals potentially high concentrations of trace metal (TM); such as V, U, Ni, Cr, Cu, and Mo, considered hazardous elements. The phosphatic wastes contain considerable amounts of these toxic elements (Boumaza et al., 2021, 2024) and are being stocked in uncontrolled sites for long periods, exposing them to erosion and weathering (Khelifi et al., 2022; Zhao et al., 2023). Subsequently, they can be easily transported, precipitated, and accumulated near living organisms, which poses environmental risks, such as water, soil and air contamination, threatening the human and animal health (Khelifi et al., 2024; Zhao et al., 2024). Thus, beside their economic benefits, exploitation of the phosphatic wastes can play a crucial role in environmental preservation.

5.4.2. *Economic importance and supply risk assessments*

A number of criteria are required to evaluate the REE potential in sedimentary phosphorite deposits. The economic importance (EI) and the supply risk (SR) are the two main assessment parameters used by the European Commission to evaluate the criticality of a raw material. The economic importance of a specific material is linked to its importance in end-use applications, as well as the availability and effectiveness of potential alternatives (Grohol and Veeh, 2023). The supply risk for the same material is closely tied to factors, such as the diversity and stability of global and EU sourcing, dependence on external sources, the political stability of supplier countries, and barriers that affect its supply chain (Grohol and Veeh, 2023). The EI/SR ratio is used in order to assess the economic importance of a given material or supply risk. The low ratio (EI/SR $<$ 1) suggests a supply risk, a EI/SR ratio in the 1 to 2 range indicates moderate economic importance, while a high ratio (EI/SR $>$ 2) addresses economic importance (Mongelli et al., 2021). On the EI/SR versus CM/CM_{UCC} diagram (where CM_{UCC} is the critical material (LREE (La—Sm) and HREE (Eu—Lu) + Y) normalized to the average Upper Continental Crust) (Fig. 13), the HREE+Y contents of phosphorites from both the northern and southern basins of the Tebessa region plot in the supply risk field; they also display clear enrichment with respect to the contents in the UCC.

However, the growing push towards electromobility has introduced new parameters for evaluating the criticality of REEs. Li et al. (2019) suggest that Nd, Dy, Ce, Pr, and La are the most critical elements among the REE. The [(Nd + Dy+Ce + Pr + La)/ΣREE+Y] ratio can, therefore, be a useful tool in conveying REEs profitability for the electromobility market (Pyrgaki et al., 2021). In this study, the percentage of critical metals for electromobility in both the northern and southern basin phosphorites is greater than 50 % of the total ΣREE+Y contents (65.7 % and 52.1 % for the southern basin and northern basin phosphorites respectively); thus, supporting the potential profitability of these phosphorite deposits.

6. Conclusion

This study investigates the poorly studied fine fraction (<45 μm) of Algerian phosphorite matrices, typically regarded as waste material. Petrographic, mineralogical, and geochemical analyses of selected phosphorites from the northern and southern basins yielded the following findings:

(1) The phosphatic particles are mainly coprolites, pellets, and glauconites, with coprolites prevailing in the north and pellets dominating the south, together with the development of the glauconitization processes, particularly at the Paleocene-Eocene transition.
(2) The phosphatic matrix comprises calcite, dolomite, carbonate fluorapatite, glauconite, quartz, chlorite and gypsum. Similar to the whole-rock, the geochemical composition of the matrix is characterized by high CaO and P_2O_5 and significantly high REY contents.

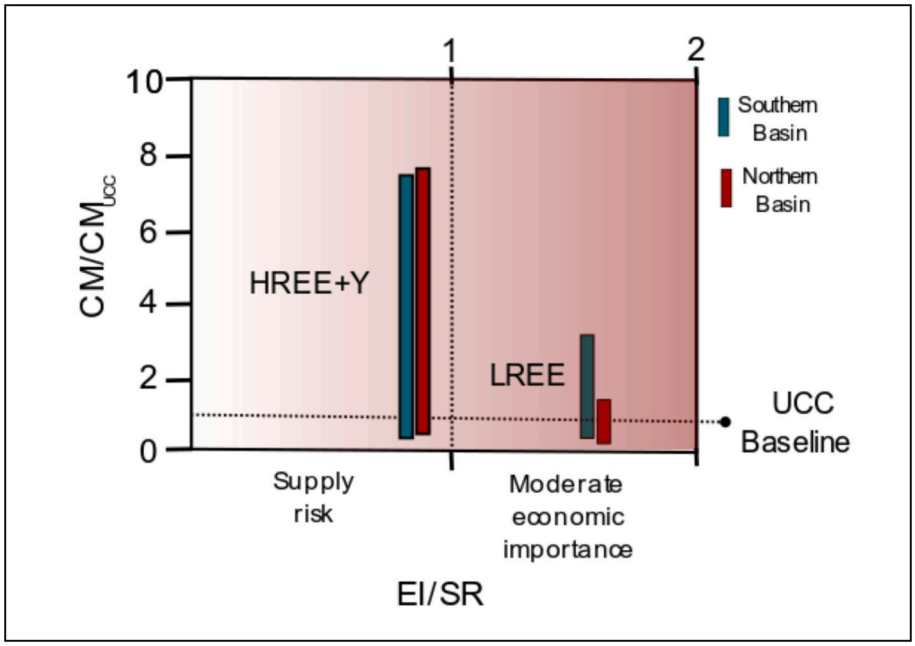

Fig. 13. LREE and HREE+Y profitability diagram: EI/SR = Economic Importance to Supply Risk ratio; CM/CMUCC = minimum–maximum range of critical metal normalized to its average UCC content.

(3) The geochemical signature of the northern basin phosphorite matrix indicates an open marine environment, with a transition from sub-oxic conditions in the bottom of the studied section to more oxygenated upper layers. In contrast, the southern basin phosphorite samples suggest a development from a restricted environment, with sub-oxic to sub-reducing conditions during the main sub-layer phosphorite deposition, towards more oxic conditions during the deposition of the upper sub-layer phosphorites. The basal sub-layer, however, reflects a distinctly reduced environment.
(4) The formation of glauconites and the development of glauconitization process in both basins indicate two contrasting sedimentation rates: rapid in the north and slow to moderate towards the south at the Paleocene–Eocene transition, which may record global warming events, within relatively open shallow waters in the north and semi-confined deep waters in the south.
(5) Regarded as phosphatic waste during exploitation / enrichment processes of the Kef Essenoun deposit, the matrix exhibits promising REY content (up to 863 ppm) and the ΣREE reaching 678 ppm, the highest REE concentrations are recorded in the glauconite-rich levels. This makes these wastes a potential secondary REE source.
(6) Considering the outlook coefficient (C_{outl}) of REE composition and the percentage of critical elements (REY_{def}) in the ΣREE, the matrix spans a range from promising (33 % $\leq REY_{def} \leq$50 %; 0.9 $\leq C_{outl} \leq$ 3.1) to highly promising ores ($REY_{def} \geq$62 % and $C_{outl} \geq$ 2.8). The ΣREE contents (exceeding 300 ppm) also meets the minimum industrial grade required for the extraction from a secondary source.
(7) The EI/SR ratio versus CM/CM_{UCC} reveals that the HREE + Y are not only characterized by supply risk, but also emerge as the most significantly enriched REE in the phosphorite deposits of both basins compared to the UCC.
(8) Since this study highlights the REY potential of the phosphorite matrices, we suggest further investigations in order to precisely assess these resources and optimize economic extraction protocols.

Nevertheless, some limitations are associated with this work. Additional isotopic data, are needed to confirm the onset of the PETM and other related Paleocene–Eocene thermal events, as well as their effects on glauconitization and REE enrichment. Moreover, estimating the quantities of matrix material and potential sludges remains challenging for accurately assessing the REE resources of the P-matrix and evaluating the economic feasibility of extraction within an environmentally sustainable framework. Therefore, further related studies are strongly recommended.

CRediT authorship contribution statement

Riadh Aouachria: Writing – review & editing, Writing – original draft, Investigation, Formal analysis, Conceptualization. **Rabah Kechiched:** Writing – review & editing, Writing – original draft, Supervision, Methodology, Investigation, Conceptualization. **Roberto Buccione:** Writing – review & editing, Writing – original draft, Investigation, Formal analysis, Data curation. **Giovanni Mongelli:** Writing – review & editing, Writing – original draft, Validation, Methodology, Formal analysis, Conceptualization. **Ouafi Ameur-Zaimeche:** Writing – review & editing, Investigation, Data curation. **Olivier Bruguier:** Validation, Methodology, Formal analysis, Conceptualization. **László Kocsis:** Writing – review & editing, Validation, Methodology, Conceptualization. **Rabah Laouar:** Writing – review & editing, Validation, Methodology, Formal analysis, Conceptualization.

Declaration of Generative AI and AI-assisted technologies in the writing process

During the preparation of this work the authors used ChatGPT (https://chatgpt.com/) in order to only enhance readability and language clarity. After using this tool/service, the authors reviewed and edited the content as needed and take full responsibility for the content of the publication.

Declaration of competing interest

The authors declare that they have no known competing financial interests or personal relationships that could have appeared to influence the work reported in this paper.

Acknowledgements

R.K. would like to thank the National Company of Phosphate (SOMIPHOS) for supplying the samples. R.K. acknowledges the University of Kasdi Merbah Ouargla for financial support facilitating short research trips to Italy. This work is part of the national Algerian research project (PRFU) under the code: E04N01UN300120230002. The authors would like to warmly thank the Editor-in-Chief, the Associate Editor, and the anonymous reviewers for their editorial handling and careful review, which greatly improved the quality of the paper.

Appendix A. Supplementary data

Supplementary data to this article can be found online at https://doi.org/10.1016/j.gexplo.2025.107889.

Data availability

Data will be made available on request.

References

Abbott, A.N., Haley, B.A., McManus, J., Reimers, C.E., 2015. The sedimentary flux of dissolved rare earth elements to the ocean. Geochim. Cosmochim. Acta 154, 186–200.
Abedini, A., Asghar Calagari, A., 2017. REEs geochemical characteristics of lower Cambrian phosphatic rocks in the Gorgan-Rasht Zone, northern Iran: implications for diagenetic effects and depositional conditions. J. Afr. Earth Sci. 135, 115–124. https://doi.org/10.1016/j.jafrearsci.2017.08.018.
Addinsoft, 2021. XLSTAT Statistical and Data Analysis Solution. New York, USA. https://www.xlstat.com.
Aitchison, J., 1986. The Statistical Analysis of Compositional Data. Chapman and Hall, London, U.K, p. 416.
Alibo, D.S., Nozaki, Y., 1999. Rare earth elements in seawater: particle association, shalenormalization, and Ce oxidation. Geochim. Cosmochim. Acta 63, 363–372. https://doi.org/10.1016/S0016-7037(98)00279-8.
Amorosi, A., 1995. Glaucony and sequence stratigraphy; a conceptual framework of distribution in siliciclastic sequences. J. Sediment. Res. 65, 419–425. https://doi.org/10.1306/D4268275-2B26-11D7-8648000102C1865D.
Arning, E.T., Birgel, D., Brunner, B., Peckmann, J., 2009. Bacterial formation of phosphatic laminites off Peru. Geobiology 7, 295–307. https://doi.org/10.1111/j.1472-4669.2009.00197.x.
Auer, G., Markus, R., Christoph, A.H., Werner, E.P., 2017. The impact of transport processes on rare earth element patterns in marine authigenic and biogenic phosphates. Geochim. Cosmochim. Acta 203, 140–156. https://doi.org/10.1016/j.gca.2017.01.001.
Baldermann, A., Dietzel, M., Mavromatis, V., Mittermayr, F., Warr, L.N., Wemmer, K., 2017. The role of Fe on the formation and diagenesis of interstratified glauconitesmectite and illite-smectite: a case study of lower cretaceous shallow-water carbonates. Chem. Geol. 453, 21–34. https://doi.org/10.1016/j.chemgeo.2017.02.008.
Banerjee, S., Bansal, U., Pande, K., Meena, S.S., 2016a. Compositional variability of glauconites within the Upper cretaceous Karai Shale Formation, Cauvery Basin, India: implications for evaluation of stratigraphic condensation. Sediment. Geol. 331, 12–29. https://doi.org/10.1016/j.sedgeo.2015.10.012.
Banerjee, S., Bansal, U., Vilas Thorat, A., 2016b. A review on palaeogeographic implications and temporal variation in glaucony composition. J. Palaeogeogr. 5 (1), 43–71. https://doi.org/10.1016/j.jop.2015.12.001.

Banerjee, S., Farouk, S., Nagm, E., Choudhury, T.R., Meena, S.S., 2019. High mg-glauconite in the Campanian Duwi formation of Abu Tartur plateau, Egypt and its implications. J. Afr. Earth Sci. 156, 12–25.
Banerjee, S., Choudhury, T.R., Saraswati, P.K., Khanolkar, S., 2020. The formation of authigenic deposits during Paleogene warm climatic intervals: a review. J. Palaeogeogr. 9 (1), 27. https://doi.org/10.1186/s42501-020-00076-8.
Bansal, U., Pande, K., Banerjee, S., Nagendra, R., Jagadeesan, K.C., 2019. The timing of oceanic anoxic events in the cretaceous succession of Cauvery Basin: Constraints from 40Ar/39Ar ages of glauconite in the Karai Shale Formation. Geol. J. 54, 308–315.
Bansal, U., Banerjee, S., Pande, K., Ruidas, D.K., 2020. Unusual seawater composition of the late cretaceous Tethys imprinted in glauconite of Narmada basin, Central India. Geol. Mag. 157, 233–247. https://doi.org/10.1017/S0016756819000621.
Bau, M., 1996. Controls on fractionation of isovalent trace elements in magmatic and aqueous systems: evidence from Y/Ho, Zr/Hf and lanthanide tetrad effect. Contrib. Mineral. Petrol. 123, 323–333. https://doi.org/10.1007/s004100050159.
Bau, M., 1999. Scavenging of dissolved yttrium and rare earths by precipitating iron oxyhydroxide: experimental evidence for Ce oxidation, Y–Ho fractionation, and lanthanide tetrad effect. Geochim. Cosmochim. Acta 63, 67–77. https://doi.org/10.1016/S0016-7037(99)00014-9.
Bau, M., Dulski, P., 1994. Evolution of the yttrium-holmium systematics of seawater through time. Mineral. Mag. 58A (1), 61–62.
Bau, M., Dulski, P., 1996. Distribution of yttrium and rare-earth elements in the Penge and Kuruman iron-formations. Transvaal Supergroup. Precambr. Res. 79, 37–55. https://doi.org/10.1016/0301-9268(95)00087-9.
Bau, M., Dulski, P., 1999. Comparing yttrium and rare earths in hydrothermal fluids from the Mid-Atlantic Ridge: implications for Y and REE behaviour during near-vent mixing and for the Y/Ho ratio of Proterozoic seawater. Chem. Geol. 155 (1–2), 77–90.
Bau, M., Möller, P., Dulski, P., 1997. Yttrium and lanthanides in eastern Mediterranean seawater and their fractionation during redox-cycling. Mar. Chem. 56 (1–2), 123–131.
Bau, M., Balan, S., Schmidt, K., Koschinsky, A., 2010. Rare earth elements in mussel shellsof the Mytilidae family as tracers for hidden and fossil high–temperature hydrothermal systems. Earth Planet. Sci. Lett. 299 (3), 310–316. https://doi.org/10.1016/j.epsl.2010.09.011.
Bayon, G., German, C.R., Burton, K.W., Nesbitt, R.W., Rogers, N., 2004. Sedimentary FeMn oxyhydroxides as paleoceanographic archives and the role of aeolian flux in regulating oceanic dissolved REE. Earth Planet. Sci. Lett. 224, 477–492.
Beji-Sassi, A., Sassi, S., 1999. Cadmium associated with phosphate deposits in southern Tunisia. J. Afr. Earth Sci. 29 (3), 501–513.
Ben Hassen, A., Trichet, J., Disnar, J.R., Belayouni, H., 2009. Données nouvelles sur le contenu organique des dépôts phosphatés du gisement de Ras-Draâ (Tunisie). Compt. Rendus Geosci. 341, 319–326. https://doi.org/10.1016/j.crte.2009.02.001.
Ben Hassen, A., Trichet, J., Disnar, J.R., 2010. Pétrographie et géochimie comparées des pellets phosphatés et de leur gangue dans le gisement phosphaté de Ras-Draaa (Tunisie). Implications sur la génèse des pellets phosphatés. Swiss J. Geosci. 103 (3), 457–473. https://doi.org/10.1007/s00015-010-0029-x.
Blès, J., Fleury, J., 1971. Carte géologique 1/50 000 Morsott (178) et notice explicative. Publication Service Géologique de l'Algérie.
Bolle, M.-P., Pardo, A., Hinrichs, K.-U., Adatte, T., Von Salis, K., Burns, S., Keller, G., Muzylev, N., 2000. The Paleocene-Eocene transition in the marginal northeastern Tethys (Kazakhstan and Uzbekistan). Int. J. Earth Sci. 89 (2), 390–414. https://doi.org/10.1007/s005310000092.
Bouabdallah, M., Elgharbi, S., Horchani-Naifer, K., Barca, D., Fattah, N., Férid, M., 2019. Chemical, mineralogical and rare earth elements distribution study of phosphorites from Sra Ouertane deposit (Tunisia). J. Afr. Earth Sci. 157, 103505.
Boumaza, B., Kechiched, R., Chekushina, T.V., 2021. Trace metal elements in phosphate rock wastes from the Djebel Onk mining area (Tébessa, eastern Algeria): a geochemical study and environmental implications. Appl. Geochem. 127, 104910.
Boumaza, B., Kechiched, R., Chekushina, T.V., Benabdeslam, N., Senouci, K., Hamitouche, A., Ait Merzeg, F., Rezgui, W., Rebouh, N.Y., Harizi, K., 2024. Geochemical distribution and environmental assessment of potentially toxic elements in farmland soils, sediments, and tailings from phosphate industrial area (NE Algeria). J. Hazard. Mater. 465, 133110.
Brock, J., Schulz-Vogt, H.N., 2011. Sulfide induces phosphate release from polyphosphate in cultures of a marine Beggiatoa strain. ISME J. 5, 497–506. https://doi.org/10.1038/ismej.2010.135.
Brookins, D.G., 1989. Aqueous geochemistry of rare earth elements. In: Lipin, B.R., McKay, G.A. (Eds.), Geochemistry and Mineralogy of Rare Earth Elements, 21. Reviews of Mineralogy, pp. 201–225.
Buccione, R., Kechiched, R., Mongelli, G., Sinisi, R., 2021. Rees in the North Africa Pbearing deposits, paleoenvironments, and economic perspectives: a review. Minerals 11 (2), 214. https://doi.org/10.3390/min11020214.
Burollet, P., Oudin, J., 1980. Paléocène er Eocène en Tunisie, pétrole et phosphates.
Byrne, R.H., Kim, K.H., 1990. Rare earth element scavenging in seawater. Geochim. Cosmochim. Acta 54 (10), 2645–2656.
Chaabani, F., 1995. Dynamique de la partie orientale du bassin de Gafsa au Crétacé et au Paléogène: Etude minéralogique et géochimique de la série phosphatée Eocène. Tunisie Méridionale. Thèse Doctrat d'Etat. Université de Tunis II, Tunis.
Chabou-Mostefai, S., 1987. Étude de la série phosphatée tertiaire du Djebel Onk, Algérie, Stratigraphie, Pétrographie, Minéralogie et Analyse Statistique, Université de Droit, d'Économie et des Sciences d'Aix-Marseille, France. In: Thèse Doctorat, p. 376.
Chafetz, H.S., Reid, A., 2000. Syndepositional shallow-water precipitation of glauconitic minerals. Sediment. Geol. 136 (1–2), 29–42.
Charbonnier, G., Puceat, E., Bayon, G., Desmares, D., Dera, G., Durlet, C., Deconinck, J. F., Amedro, F., Gourlan, A.T., Pellenard, P., Bomou, B., 2012. Reconstruction of the Nd isotope composition of seawater on epicontinental seas: testing the potential of Fe-Mn oxyhydroxide coatings on foraminifera tests for deep-time investigations. Geochim. Cosmochim. Acta 99, 39–56.
Chattoraj, S.L., Banerjee, S., Saraswati, P.K., Bansal, U., 2016. Origin, depositional setting and stratigraphic implications of Palaeogene glauconite of Kutch. Recent Studies on the Geology of Kachchh 75–88. https://doi.org/10.17491/cgsi/2016/105413.
Christmann, P., 2014. A forward look into rare earth supply and demand: a role for sedimentary phosphate deposits? Procedia Eng. 83, 19–26.
Cielensky, S., Benchernine, N., Watkowski, T., 1988. Works of prospecting and assessment of phosphates in the region of Bir El Ater. Internal report, EREM (Entreprise de Recherche et d'Exploration Minière)..
Ciobotă, V., Salama, W., Jentzsch, P.V., Tarcea, N., Rösch, P., El Kammar, A., et al., 2014. Raman investigations of Upper cretaceous phosphorite and black shale from Safaga District, Red Sea, Egypt. Spectrochim. Acta A Mol. Biomol. Spectrosc. 118, 42–47.
Clay Kelly, D., Bralower, T.J., Zachos, J.C., Silva, I.P., Thomas, E., 1996. Rapid diversification of planktonic foraminifera in the tropical Pacific (ODP site 865) during the late Paleocene thermal maximum. Geology 24 (5), 423–426.
Clocchiatti, R., Sassi, S., 1972. Découverte d'un témoin d'un volcanisme Paléocène éocène dans le bassin phosphate de Métlaoui (Tunisie méridionale). C. R. Acad. Sci. Paris 324, 205e212.
Comas-Cufí, M., Thió-Henestrosa, S., 2011. CoDaPack 2.0: A stand-alone, multi-platform compositional software. In: Egozcue, J.J., Tolosana-Delgado, R., Ortego, M.I. (Eds.), CoDaWork'11: 4th International Workshop on Compositional Data Analysis. Sant Feliu de Guíxols.
Cramer, B.S., Wright, J.D., Kent, D.V., Aubry, M.P., 2003. Orbital climate forcing of δ13C excursions in the late Paleocene–early Eocene (chrons C24n–C25n). Paleoceanography 18 (4). https://doi.org/10.1029/2003PA000909.
Dass Amiour, M., Mezghache, H., Elouadi, B., 2013. The use of three physico-chemical methods in the study of the organic matter associated with the sedimentary phosphorites in Djebel Onk Basin Algeria. Arab. J. Geosci. 6, 309–319. https://doi.org/10.1007/s12517-011-0381-9.
Dass amiour, M., Mezghache, H., Raji, O., Bodinier, J.L., 2021. Depositional environment of the Kef Essennoun phosphorites (northeastern Algeria) as revealed by P2O5 modeling and sedimentary data. Arab. J. Geosci. 14 (12), 1–17.
De Baar, H.J.W., Bacon, M.P., Brewer, P.G., Bruland, K.W., 1985. Rare-earth elements in the Pacific and Atlantic oceans. Geochim. Cosmochim. Acta 49, 1943–195.
De Baar, H.J.W., German, C.R., Elderfield, H., Van Gaans, P., 1988. Rare earth element distributions in anoxic waters of the Cariaco Trench. Geochim. Cosmochim. Acta 52, 1203–1219. https://doi.org/10.1016/0016-7037(88)90275-X.
De Carlo, E.H., Green, W.J., 2002. Rare earth elements in the water column of Lake Vanda, McMurdo Dry Valleys. Antarctica. Geochim. Cosmochim. Acta 66, 1323–1333. https://doi.org/10.1016/S0016-7037(01)00861-4.
De Conto, R.M., Galeotti, S., Pagani, M., Tracy, D., Schaefer, K., Zhang, T., Pollard, D., Beerling, D.J., 2012. Past extreme warming events linked to massive carbon release from thawing permafrost. Nature 484 (7392), 87–91.
Diab, I., Laouar, R., Bosch, D., Tlili, A., Degaichia, A., Bruguier, O., Zaabat, M., Bouhlel, S., Kechiched, R., 2024. The Ain Dibba and Ain Kissa phosphorites, Tebessa (NE Algeria): REE depletion versus shallow, open depositional environment during the Paleocene-Eocene phosphogenesis in North Africa. J. Afr. Earth Sci. 220, 105433. https://doi.org/10.1016/j.jafrearsci.2024.105433.
Dickens, G.R., O'Neil, J.R., Rea, D.K., Owen, R.M., 1995. Dissociation of oceanic methane hydrate as a cause of the carbon isotope excursion at the end of the Paleocene. Paleoceanography 10 (6), 965–971.
Dubourdieu, G., 1956. Etude structurale et intérêt pétrolier de l'Ouenza (Confins algéro-tunisien). Bull. Serv. Géol. Algér. 10, 659.
Dumoulin, J.A., Slack, J.F., Whalen, M.T., Harris, A.G., 2011. Depositional Setting and Geochemistry of Phosphorites and Metalliferous Black Shales in the Carboniferous-Permian Lisburne Group. northern Alaska (No. 1776-C). US Geological Survey.
Durozoy, M.G., 1956. Carte géologique de l'Algérie au 1/50000, feuille n° 206 Tébessa, avec notice explicative détaillée. Publication du Service de la Carte géologique de l'Algérie.
Ebrahimi, P., Albanese, S., Esposito, L., Zuzolo, D., Cicchella, D., 2021. Coupling compositional data analysis (CoDA) with hierarchical cluster analysis (HCA) for preliminary understanding of the dynamics of a complex water distribution system: the Naples (South Italy) case study. Environ. Sci.: Water Res. Technol. 7 (6), 1060–1077.
El Albani, A., Meunier, A., Fursich, F., 2005. Unusual occurrence of glauconite in a shallow lagoonal environment (lower cretaceous, northern Aquitaine Basin, SW France). Terra Nova 17, 537–544. https://doi.org/10.1111/j.1365-3121.2005.00646.x.
El Zrelli, R., Rabaoui, L., Abda, H., Daghbouj, N., Pérez-López, R., Castet, S., Aigouy, T., Bejaoui, N., Courjault-Radé, P., 2019. Characterization of the role of phosphogypsum foam in the transport of metals and radionuclides in the Southern Mediterranean Sea. J. Hazard. Mater. 363, 258–267.
Emsbo, P., McLaughlin, P.I., Breit, G.N., du Bray, E.A., Koenig, A.E., 2015. Rare earth elements in sedimentary phosphate deposits: solution to the global REE crisis. Gondwana Res. 27 (2), 776–785.
Ettoumi, M., Jouini, M., Neculita, C.M., Bouhlel, S., Coudert, L., Haouech, I., Benzaazoua, M., 2020. Characterization of Kef Shfeir phosphate sludge (Gafsa, Tunisia) and optimization of its dewatering. J. Environ. Manag. 254, 109801. https://doi.org/10.1016/j.jenvman.2019.109801.
Fazio, A.M., Scasso, R.A., Castro, L.N., Carey, S., 2007. Geochemistry of rare earth elements in early-diagenetic miocene phosphatic concretions of Patagonia,

Argentina: phosphogenetic implications. Deep-Sea Res. II 54, 1414–1432. https://doi.org/10.1016/j.dsr2.2007.04.013.
Ferhaoui, S., Kechiched, R., Bruguier, O., Sinisi, R., Kocsis, L., Mongelli, G., Bosch, D., Ameur-Zaimeche, O., Laouar, R., 2022. Rare earth elements plus yttrium (REY) in phosphorites from the Tébessa region (Eastern Algeria): Abundance, geochemical distribution through grain size fractions, and economic significance. J. Geochem. Explor. 241, 107058. https://doi.org/10.1016/j.gexplo.2022.107058.
Ferrow, E., Vajda, V., Koch, C.B., Peucker-Ehrenbrink, B., Willumsen, P.S., 2011. Multiproxy analysis of a new terrestrial and a marine Cretaceous–Paleogene (K–Pg) boundary site from New Zealand. Geochim. Cosmochim. Acta 75 (2), 657–672. https://doi.org/10.1016/j.gca.2010.10.016.
Föllmi, K.B., 1996. The Phosphorus Cycle, Phosphogenesis Phosphate-Rich Deposits 40, 55–124. https://doi.org/10.1016/0012-8252(95)00049-6.
Fourine, D., 1980. Phosphates et pétrole en Tunisie, Mém..
Galfati, I., Sassi, A.B., Zaier, A., Bouchardon, J.L., Bilal, E., Joron, J.L., Sassi, S., 2010. Geochemistry and mineralogy of Paleocene–Eocene Oum El Khecheb phosphorites (Gafsa Metlaoui Basin) Tunisia. Geochem. J. 44, 189–210. https://doi.org/10.2343/geochemj.1.0062.
Garcia-Solsona, E., Jeandel, C., Labatut, M., Lacan, F., Vance, D., Chavagnac, V., Pradoux, C., 2014. Rare earth elements and Nd isotopes tracing water mass mixing and particle-seawater interactions in the SE Atlantic. Geochim. Cosmochim. Acta 125, 351–372.
Garnit, H., Bouhlel, S., Barca, D., Chtara, C., 2012. Application of LA-ICP-MS to sedimentary phosphatic particles from Tunisian phosphorite deposits: insights from trace elements and REE into paleo-depositional environments. Chem. Erde 72, 127–139. https://doi.org/10.1016/j.chemer.2012.02.001.
Garnit, H., Bouhlel, S., Jarvis, I., 2017. Geochemistry and depositional environments of Paleocene–Eocene phosphorites: Metlaoui Group, Tunisia. J. Afr. Earth Sci. 134, 704–736. https://doi.org/10.1016/j.jafrearsci.2017.07.021.
Garrles, R.M., Christ, C.I., 1965. Solution, Minerals and Equilibria. Harper and Row, New York, p. 450 n.4.
Geological Survey, U.S., 2024. Mineral commodity summaries 2024: U.S. Geological Survey 212. https://doi.org/10.3133/mcs2024.
German, C.R., Elderfield, H., 1990. Application of the Ce anomaly as a paleoredox indicator: the ground rules. Paleoceanography 5, 823–833.
German, C.R., Holliday, B.P., Elderfield, H., 1991. Redox cycling of rare earth elements in the suboxic zone of the Black Sea. Geochim. Cosmochim. Acta 55, 3553–3558. https://doi.org/10.1016/0016-7037(91)90055-A.
Glenn, C.R., Arthur, M.A., 1988. Petrology and major element geochemistry of Peru margin phosphorites and associated diagenetic minerals: Authigenesis in modern organic-rich sediments. Mar. Geol. 80 (3–4), 231–267.
Gnandi, K., Tobschall, H.J., 2003. Distribution patterns of rare-earth elements and uranium in tertiary sedimentary phosphorites of Hahotoé Kpogamé, Togo. J. Afr. Earth Sci. 37, 1–10. https://doi.org/10.1016/j.jafrearsci.2003.08.002.
Goldhammer, T., Brunner, B., Bernasconi, S.M., Ferdelman, T.G., Zabel, M., 2011. Phosphate oxygen isotopes: Insights into sedimentary phosphorus cycling from the Benguela upwelling system. Geochim. Cosmochim. Acta 75, 3741–3756. https://doi.org/10.1016/j.gca.2011.04.006.
Grohol, M., Veeh, C., 2023. In: European Commission (Ed.), Study on the critical raw materials for the EU final Report, p. 158. https://data.europa.eu/doi/10.2873/725585.
Haley, B.A., Klinkhammer, G.P., McManus, J., 2004. Rare earth elements in porewaters of marine sediments. Geochim. Cosmochim. Acta 68, 1265–1279. https://doi.org/10.1016/j.gca.2003.09.012.
Hou, X.Z., Yang, Z.F., Wang, Z.J., 2020. The occurrence characteristics and recovery potential of middle-heavy rare earth elements in the Bayan Obo deposit, Northern China. Ore Geol. Rev. J. Hazard. Mater. 126 (465), 103737, 133110.
Huggett, J., Adetunji, J., Longstaffe, F., Wray, D., 2017. Mineralogical and geochemical characterisation of warm-water, shallow-marine glaucony from the Tertiary of the London Basin. Clay Miner. 52 (1), 25–50. https://doi.org/10.1180/claymin.2017.052.1.02.
Jaireth, S., Hoatson, D.M., Miezitis, Y., 2014. Geological setting and resources of the major rare-earth-element deposits in Australia. Ore Geol. Rev. 62, 72–128.
Ji, B., Li, Q., Tang, H., Zhang, W., 2022. Rare earth elements (REEs) recovery from coal waste of the Western Kentucky no. 13 and Fire Clay seams. Part II: re-investigation on the effect of calcination. Fuel 315, 123145. https://doi.org/10.1016/j.fuel.2022.123145.
John, C.M., Bohaty, S.M., Zachos, J.C., Sluijs, A., Gibbs, S., Brinkhuis, H., Bralower, T.J., 2008. North American continental margin records of the Paleocene-Eocene thermal maximum: implications for global carbon and hydrological cycling: CONTINENTAL MARGIN RECORDS OF THE PETM. Paleoceanography 23 (2). https://doi.org/10.1029/2007PA001465 n/a-n/a.
Kechiched, R., 2017. Les phosphates du nord de Tébessa (Dyr et Elkouif): étude sédimentologique, gitologique et géochimique. Université Badji (Mokhtar-Annaba)..
Kechiched, R., Laouar, R., Bruguier, O., Salmi-Laouar, S., Ameur-Zaimeche, O., Foufou, A., 2016. Preliminary data of REE in Algerian phosphorites: a comparative study and paleo-redox insights. Procedia Eng. 138, 19–29. https://doi.org/10.1016/j.proeng.2016.02.048.
Kechiched, R., Laouar, R., Bruguier, O., Salmi-Laouar, S., Kocsis, L., Bosch, D., Foufou, A., Ameur-Zaimeche, O., Larit, H., 2018. Glauconite-bearing sedimentary phosphorites from the Tébessa region (eastern Algeria): evidence of REE enrichment and geochemical constraints on their origin. J. Afr. Earth Sci. 145, 190–200. https://doi.org/10.1016/j.jafrearsci.2018.05.018.
Kechiched, R., Laouar, R., Bruguier, O., Kocsis, L., Salmi-Laouar, S., Bosch, D., Ameur-Zaimeche, O., Foufou, A., Larit, H., 2020. Comprehensive REE + Y and sensitive redox trace elements of Algerian phosphorites (Tébessa, eastern Algeria): a geochemical study and depositional environments tracking. J. Geochem. Explor. 208, 106396. https://doi.org/10.1016/j.gexplo.2019.106396.
Kechiched, R., Sinisi, R., Kocsis, L., Bruguier, O., Mongelli, G., Ferhaoui, S., Bosch, D., Ameur-Zaimeche, O., Buccione, R., Laouar, R., 2024. Phosphate Deposits in North Africa: an Overview of Algerian-Tunisian Deposits, Geochemistry and Paleoenvironments. The Geology of North Africa 471–499. https://doi.org/10.1007/978-3-031-48299-1_15.
Khan, S.A., Khan, K.F., Dar, S.A., 2016. Ree geochemistry of early Cambrian phosphorites of Masrana and Kimoi blocks, Uttarakhand, India. Arab. J. Geosci. 9, 1–10. https://doi.org/10.1007/s12517-016-2477-8.
Khelifi, F., Batool, S., Kechiched, R., Padoan, E., Ncibi, K., Hamed, Y., 2024. Abundance, distribution, and ecological/environmental risks of critical rare earth elements (REE) in phosphate ore, soil, tailings, and sediments: application of spectroscopic fingerprinting. J. Soils Sediments 24 (5), 2099–2118. https://doi.org/10.1007/s11368-024-03771-4.
Kocsis, L., Ounis, A., Chaabani, F., Salah, N.M., 2013. Paleoenvironmental conditions and strontium isotope stratigraphy in the Paleogene Gafsa Basin (Tunisia) deduced from geochemical analyses of phosphatic fossils. Int. J. Earth Sci. 102, 1111–1129. https://doi.org/10.1007/s00531-012-0845-5.
Kocsis, L., Ounis, A., Baumgartner, C., Pirkenseer, C., Harding, I.C., Adatte, T., Chaabani, F., Mohamed, S., 2014. Paleocene–Eocene palaeoenvironmental conditions of the main phosphorite deposits (Chouabine Formation) in the Gafsa Basin, Tunisia. J. Afr. Earth Sci. 100, 586–597. https://doi.org/10.1016/j.jafrearsci.2014.07.024.
Khelifi, F., Mokadem, N., Liu, G., Yousaf, B., Zhou, H., Ncibi, K., Hamed, Y., 2022. Occurrence, contamination evaluation and health risks of trace metals within soil, sediments and tailings in southern Tunisia. Int. J. Environ. Sci. Technol. 19, 6127–6140. https://doi.org/10.1007/s13762-021-03531-8.
Kocsis, L., Gheerbrant, E., Mouflih, M., Cappetta, H., Ulianov, A., Chiaradia, M., Bardet, N., 2016. Gradual changes in upwelled seawater conditions (redox, pH) from the late cretaceous through early Paleogene at the northwest coast of Africa: negative Ce anomaly trend recorded in fossil bio-apatite. Chem. Geol. 421, 44–54. https://doi.org/10.1016/j.chemgeo.2015.12.001.
Koeppenkastrop, D., De Carlo, E.H., 1992. Sorption of rare-earth elements from seawater onto synthetic mineral particles: an experimental approach. Chem. Geol. 95, 251–263.
Koschinsky, A., Stascheit, A., Bau, M., Halbach, P., 1997. Effects of phosphatization on the geochemical and mineralogical composition of marine ferromanganese crusts. Geochim. Cosmochim. Acta 61 (19), 4079–4094.
Krajewski, K.P., 1994. Biological processes and apatite formation in sedimentary environments. Ecol. Geol. Helv. 87, 701–745.
Laouar, K., Laouar, R., Bruguier, O., Bosch, D., Kechiched, R., Bouhlel, S., Tlili, A., 2024. Geochemistry of Bled El Hadba phosphorites (NE Algeria): Glauconitization process versus REE-enrichment. J. Geochem. Explor. 258, 107398. https://doi.org/10.1016/j.gexplo.2024.107398.
Li, X.Y., Ge, J.P., Chen, W.Q., Wang, P., 2019. Scenarios of rare earth elements demand driven by automotive electrification in China: 2018–2030. Resour. Conserv. Recycl. 145, 322–331.
Lourens, L.J., Sluijs, A., Kroon, D., Zachos, J.C., Thomas, E., Röhl, U., Bowles, J., Raffi, I., 2005. Astronomical pacing of late Palaeocene to early Eocene global warming events. Nature 435, 1083–1087.
Lucas, J., Prevot-Lucas, L., 1995. Tethyan phosphates and bioproductites. In: Nairn, A.E., et al. (Eds.), The Ocean Basins and Margins—The Tethys Ocean, 8. Plenum Press, New York, pp. 367–391.
Lumiste, K., Mänd, K., Bailey, J., Stüeken, E.E., Paiste, K., Lang, L., Kirsimäe, K., 2021. Constraining the conditions of phosphogenesis: Stable isotope and trace element systematics of recent Namibian phosphatic sediments. Geochim. Cosmochim. Acta 302, 141–159.
Mänd, K., Kirsimäe, K., Lepland, A., Crosby, C.H., Bailey, J.V., Konhauser, K.O., Wirth, R., Schreiber, A., Lumiste, K., 2018. Authigenesis of biomorphic apatite particles from Benguela upwelling zone sediments off Namibia: the role of organic matter in sedimentary apatite nucleation and growth. Geobiology 1–19. https://doi.org/10.1111/gbi.12309.
McInerney, F.A., Wing, S.L., 2011. The Paleocene-Eocene thermal maximum: a perturbation of carbon cycle, climate, and biosphere with implications for the future. Annu. Rev. Earth Planet. Sci. 39, 489–516.
McLennan, S.M., 1989. Rare earth elements in sedimentary rocks: influence of provenance and sedimentary processes. In: Lipin, B.R., McKay, G.A. (Eds.), Geochemistry and Mineralogy of rare Earth elements. Rev. Mineral, 21, pp. 169–200.
Merkle, A.B., Slaughter, M., 1968. Determination and refinement of the structure of heulandite. Am. Mineral. 53 (7–8), 1120–1138.
Michard, A., Albarede, F., Michard, G., Minster, J.F., Charlou, J.L., 1983. Rare-earth elements and uranium in high-temperature solutions from East Pacific rise hydrothermal vent field (13 degree N). Nature 303, 795–797.
Moffett, J.W., 1990. Microbially mediated cerium oxidation in sea water. Nature 345, 421–423. https://doi.org/10.1038/345421a0.
Mongelli, G., Sinisi, R., Paternoster, M., Perri, F., 2018. REEs and U distribution in P-rich nodules from Gelasian Apulian Tethyan carbonate: a genetic record. J. Geochem. Explor. 194, 19–28.
Mongelli, G., Mameli, P., Sinisi, R., Buccione, R., Oggiano, G., 2021. REEs and other critical raw materials in cretaceous Mediterranean-type bauxite: the case of the Sardinian ore (Italy). Ore Geol. Rev. 139, 104559. https://doi.org/10.1016/j.oregeorev.2021.104559.
Morad, S., Felitsyn, S., 2001. Identification of primary Ce-anomaly signatures in fossil biogenic apatite: implication for the Cambrian oceanic anoxia and phosphogenesis. Sediment. Geol. 143, 259–264. https://doi.org/10.1016/S0037-0738(01)00093-8.

Ni, P., Zhou, J., Chi, Z., Pan, J.-Y., Li, S.-N., Ding, J.-Y., Han, L., 2020. Carbonatite dyke and related REE mineralizationin the Bayan Obo REE ore field, North China: evidence from geochemistry, C-O isotopes and Rb-Sr dating. J. Geochem. Explor. 215, 106560. https://doi.org/10.1016/j.gexplo.2020.106560.
Nicolo, M.J., Dickens, G.R., Hollis, C.J., Zachos, J.C., 2007. Multiple early Eocene hyperthermals: their sedimentary expression on the New Zealand continental margin and in the deep sea. Geology 35, 699–702.
Notholt, A.J.G., 1980. Economic phosphatic sediments: mode of occurrence and stratigraphical distribution. J. Geol. Soc. Lond. 137 (6), 793–805. https://doi.org/10.1144/gsjgs.137.6.0793.
Notholt, A.J.G., Sheldon, R.P., Davidson, D.F., 1989. In: Phosphate Deposits of the World 2: Phosphate Rock Resources. Cambridge University Press, Cambridge, p. 566.
Odin, G.S., Fullagar, P.D., 1988. Chapter C4 geological significance of the glaucony facies. In: Developments in sedimentology, 45, pp. 295–332. https://doi.org/10.1016/S0070-4571(08)70069-4.
Odin, G.S., Matter, A., 1981. De glauconiarum origine. Sedimentology 28 (5), 611–641. https://doi.org/10.1111/j.1365-3091.1981.tb01925.x.
ORGM, 2000. Carte géologique de l'Algérie 1/50000 Bir El Ater (327). Publication Service Géologique de l'Algérie.
Osborne, A.H., Haley, B.A., Hathorne, E.C., Plancherel, Y., Frank, M., 2015. Rare earth element distribution in Caribbean seawater: continental inputs versus lateraltransport of distinct REE compositions in subsurface water masses. Mar. Chem. 177, 172–183.
Ounis, A., Kocsis, L., Chaabani, F., Pfeifer, H.R., 2008. Rare earth elements and stable isotope geochemistry (δ13C and δ18O) of phosphorite deposits in the Gafsa Basin, Tunisia. Palaeogeogr. Palaeoclimatol. Palaeoecol. 268, 1–18. https://doi.org/10.1016/j.palaeo.2008.07.005.
Palmer, M.R., Elderfield, H., 1986. Rare-earth elements and neodymium isotopes in ferromanganese oxide coatings of Cenozoic foraminifera from the Atlantic Ocean. Geochim. Cosmochim. Acta 50, 409–417.
Peiravi, M., Dehghani, F., Ackah, L., Baharlouei, A., Godbold, J., Liu, J., Mohanty, M., Ghosh, T., 2020. A review of rare-earth elements extraction with emphasis on nonconventional sources: coal and coal byproducts, iron ore tailings, apatite, and phosphate byproducts. Min. Metall. Explor. 38, 1–26. https://doi.org/10.1007/s42461-020-00307-5.
Peters, S.E., Gaines, R.R., 2012. Formation of the ' Great Unconformity' as a trigger for the Cambrian explosion. Nature 484, 363–366. https://doi.org/10.1038/nature10969.
Piepgras, D.J., Jacobsen, S.B., 1992. The behavior of rare earth elements in seawater: precise determination of variations in the North Pacific water column. Geochim. Cosmochim. Acta 56, 1851–1862.
Pryor, W.A., 1975. Biogenic sedimentation and alteration of argillaceous sediments in shallow marine environments. Geol. Soc. Am. Bull. 86 (9), 1244–1254.
Pyrgaki, K., Gemeni, V., Karkalis, C., Koukouzas, N., Koutsovitis, P., Petrounias, P., 2021. Geochemical occurrence of rare earth elements in mining waste and mine water: a review. Minerals 11 (8), 860.
Reynard, B., Lécuyer, C., Grandjean, P., 1999. Crystal-chemical controls on rare-earth element concentrations in fossil biogenic apatites and implications for paleoenvironmental reconstructions. Chem. Geol. 155 (3–4), 233–241.
Röhl, U., Westerhold, T., Bralower, T.J., Zachos, J.C., 2007. On the duration of the Paleocene-Eocene thermal maximum (PETM). Geochem. Geophys. Geosyst. 8 (12).
Roy Choudhury, T., Banerjee, S., Khanolkar, S., Saraswati, P.K., Meena, S.S., 2021. Glauconite authigenesis during the onset of the Paleocene-Eocene thermal Maximum: a case study from the Khuiala Formation in Jaisalmer Basin, India. Palaeogeogr. Palaeoclimatol. Palaeoecol. 571, 110388. https://doi.org/10.1016/j.palaeo.2021.110388.
Salama, W., El Kammar, A., Saunders, M., Morsy, R., Kong, C., 2015. Microbial pathways and paleoenvironmental conditions involved in the formation of phosphorite grains, Safaga District, Egypt. Sediment. Geol. 325, 41–58.
Salama, W., Khirekesh, Z., Amini, A., Shafiei Bafti, B., 2018. Diagenetic evolution of the upper Devonian phosphorites, Alborz Mountain Range, northern Iran. Sediment. Geol. 376, 90–112.
Samanta, A., Bera, M.K., Ghosh, R., Bera, S., Filley, T., Pande, K., Rathore, S.S., Rai, J., Sarkar, A., 2013. Do the large carbon isotopic excursions in terrestrial organic matter across Paleocene–Eocene boundary in India indicate intensification of tropical precipitation? Palaeogeogr. Palaeoclimatol. Palaeoecol. 387, 91–103. https://doi.org/10.1016/j.palaeo.2013.07.008.
Sassi, S., 1974. La sedimentation phosphatée au Paléocène dans le Sud et le Centre Ouest de la Tunisie. Thèse Doctorat Université. Paris Sud Orsay, France..
Schmidt, K., Koschinsky, A., Garbe-Schönberg, D., Carvalho, L.M.D., Seifert, R., 2007. Geochemistry of hydrothermal fluids from the ultramafic-hosted Logatchev hydrothermal field, 15°N on the Mid-Atlantic Ridge: temporal and spatial investigation. Chem. Geol. 242 (1–2), 1–21. https://doi.org/10.1016/j.chemgeo.2007.01.023.
Schulz, H., Schulz, H.N., 2005. Large Sulfur Bacteria and the Formation of Phosphorite. Science 80 (307), 416–418. https://doi.org/10.1126/science.1103096.
Seredin, V.V., 2010. A new method for primary evaluation of the outlook for rare earth element ores. Geol. Ore Deposits 52 (5), 428–433.
Seredin, V.V., Dai, S., 2012. Coal deposits as potential alternative sources for lanthanides and yttrium. Int. J. Coal Geol. 94, 67–93. https://doi.org/10.1016/j.coal.2011.11.001.
Sheldon, R.P., 1987. Association of phosphatic and siliceous marine sedimentary deposits. In: Hein, J.R. (Ed.), Siliceous Sedimentary Rock-Hosted Ores and Petroleum. Van Norstrand Reinhold Co, New York, pp. 58–80.
Shields, G., Stille, P., 2001. Diagenetic constraints on the use of cerium anomalies as palaeoseawater redox proxies: an isotopic and REE study of Cambrian phosphorites. Chem. Geol. 175, 29–48. https://doi.org/10.1016/S0009-2541(00)00362-4.
Shimizu, H., Tachikawa, K., Masuda, A., Nozaki, Y., 1994. Cerium and neodymium isotope ratios and REE patterns in seawater from the North Pacific Ocean. Geochim. Cosmochim. Acta 58, 323–333.
Sluijs, A., Van Roij, L., Harrington, G.J., Schouten, S., Sessa, J.A., LeVay, L.J., Reichart, G.-J., Slomp, C.P., 2014. Warming, euxinia and sea level rise during the Paleocene–Eocene Thermal Maximum on the Gulf Coastal Plain: implications for ocean oxygenation and nutrient cycling. Clim. Past 10 (4), 1421–1439. https://doi.org/10.5194/cp-10-1421-2014.
Somma, R., Ebrahimi, P., Troise, C., De Natale, G., Guarino, A., Cicchella, D., Albanese, S., 2021. The first application of compositional data analysis (CoDA) in a multivariate perspective for detection of pollution source in sea sediments: the Pozzuoli Bay (Italy) case study. Chemosphere 274, 129955.
Stalder, M., Rozendaal, A., 2004. Apatite nodules as an indicator of depositional environment and ore genesis for the Mesoproterozoic Broken Hill-type Gamsberg Zn–Pbdeposit, Namaqua Province, South Africa. Mineral. Deposita 39 (2), 189–203. https://doi.org/10.1007/s00126-003-0394-8.
Stap, L., Lourens, L.J., Thomas, E., Sluijs, A., Bohaty, S., Zachos, J.C., 2010. High-resolution deep-sea carbon and oxygen isotope records of Eocene thermal maximum 2 and H2. Geology 38, 607–610.
Stassen, P., Thomas, E., Speijer, R.P., 2015. Paleocene–Eocene thermal maximum environmental change in the New Jersey Coastal Plain: benthic foraminiferal biotic events. Mar. Micropaleontol. 115, 1–23. https://doi.org/10.1016/j.marmicro.2014.12.001.
Svensen, H., Planke, S., Malthe-Sorenssen, A., Jamtveit, B., Myklebust, R., et al., 2004. Release of methane from a volcanic basin as a mechanism for initial Eocene global warming. Nature 429, 542–545.
Svensen, H., Planke, S., Corfu, F., 2010. Zircon dating ties NE Atlantic sill emplacement to initial Eocene global warming. J. Geol. Soc. Lond. 167, 433–436.
Tahar-Belkacem, N., Ameur-Zaimeche, O., Kechiched, R., Ouladmansour, A., Heddam, S., Wood, D.A., Buccione, R., Mongelli, G., 2024. Machine learning models to predict rare earth elements distribution in Tethyan phosphate ore deposits: geochemical and depositional environment implications. Geochemistry, 126128. https://doi.org/10.1016/j.chemer.2024.126128.
Tahri, T., Bouzenzana, A., Bezzi, N., 2019. Characterization and homogenization of Bled El-Hadba phosphate ore, case of Djebel Onk (Algeria). Nauk. Visnyk NHU 2, 28–35. https://doi.org/10.29202/nvngu/2019-2/4.
Taylor, S.R., McLennan, S.M., 1985. The Continental Crust: Its Composition and Evolution. Blackwell, Oxford, p. 312.
Thiombane, M., Martín-Fernández, J.A., Albanese, S., Lima, A., Doherty, A., De Vivo, B., 2018. Exploratory analysis of multi-element geochemical patterns in soil from the Sarno River Basin (Campania region, southern Italy) through compositional data analysis (CODA). J. Geochem. Explor. 195, 110–120.
Thomas, D.J., Bralower, T.J., Zachos, J.C., 1999. New evidence for subtropical warming during the late Paleocene thermal maximum: stable isotopes from Deep Sea Drilling Project Site 527, Walvis Ridge. Paleoceanography 14 (5), 561–570. https://doi.org/10.1029/1999PA900031.
Tostevin, R., Shields, G.A., Tarbuck, G.M., He, T., Clarkson, M.O., Wood, R.A., 2016. Effective use of cerium anomalies as a redox proxy in carbonate-dominated marine settings. Chem. Geol. 438, 146–162. https://doi.org/10.1016/j.chemgeo.2016.06.027.
Tricca, A., Stille, P., Steinmann, M., Kiefel, B., Samuel, J., Eikenberg, J., 1999. Rare earth elements and Sr and Nd isotopic compositions of dissolved and suspended loads from small river systems in the Vosges mountains (France), the river Rhine and groundwater. Chem. Geol. 160 (1–2), 139–158.
Valetich, M., Zivak, D., Spandler, C., Degeling, H., Grigorescu, M., 2022. REE enrichment of phosphorites: an example of the Cambrian Georgina Basin of Australia. Chem. Geol. 588, 120654. https://doi.org/10.1016/j.chemgeo.2021.120654.
Van Houten, F.B., Purucker, M.E., 1984. Glauconitic peloids and chamositic ooids -favorable factors, constraints, and problems. Earth Sci. Rev. 20, 211–243. https://doi.org/10.1016/0012-8252(84)90002-3.
Velde, B., 2014. Green clay minerals, 9.12. In: Holland, H., Turekian, K. (Eds.), Treatise on Geochemistry, second ed. 9. Elsevier Ltd., Amsterdam, Netherlands, p. 351. e364. Sediments, diagenesis and sedimentary rocks.
Westerhold, T., Rohl, U., McCarren, H.K., Zachos, J.C., 2009. Latest on the absolute age of the Paleocene-Eocene thermal Maximum (PETM): new insights from exact stratigraphic position of key ash layers +19 and −17. Earth Planet. Sci. Lett. 287, 412–419.
Winnock, E., 1980. Les dépôts de l'Eocène au Nord de l'Afrique: Aperçu paléogéographique de l'ensemble.
Wright, J., Seymour, R.S., Shaw, H.F., 1984. REE and Nd isotopes in conodont apatite: variations with geological age and depositional environment. In: Clark, D.L. (Ed.), Conodont Biofacies and Provincialism, 196. Geol. Soc. Am. Special Paper, pp. 325–340.
Wright, J., Schrader, H., Holser, W.T., 1987. Paleoredox variations in ancient oceans recorded by rare earth elements in fossil apatite. Geochim. Cosmochim. Acta 51, 631–644. https://doi.org/10.1016/0016-7037(87)90075-5.
Wu, S., Wang, L., Zhao, L., Zhang, P., El-Shall, H., Moudgil, B., Huang, X., Zhang, L., 2018. Recovery of rare earth elements from phosphate rock by hydrometallurgical processes–a critical review. Chem. Eng.J. 335, 774–800.
Xie, Y., Li, Y., Hou, Z., Cooke, D.R., Danyushevsky, L., Dominy, S.C., Yin, S., 2015. A model for carbonatite hosted REE mineralisation — the Mianning–Dechang REE belt, Western Sichuan Province. China. Ore Geol. Rev. 70, 595–612. https://doi.org/10.1016/j.oregeorev.2014.10.027.

Xu, C., Campbell, I.H., Kynicky, J., Allen, C.M., Chen, Y., Huang, Z., Qi, L., 2008. Comparison of the Daluxiang and Maoniuping carbonatitic REE deposits with Bayan Obo REE deposit, China. Lithos 106 (12), 12–24. https://doi.org/10.1016/j.lithos.2008.06.005.

Zachos, J.C., Pagani, M., Sloan, L., Thomas, E., Billups, K., 2001. Trends, rhythms, and aberrations in global climate 65 Ma to present. Science 292, 686–693.

Zachos, J.C., Röhl, U., Schellenberg, S.A., Sluijs, A., Hodell, D.A., Kelly, D.C., Thomas, E., Nicolo, M., Raffi, I., Lourens, L.J., McCarren, H., Kroon, D., 2005. Rapid Acidification of the Ocean during the Paleocene-Eocene thermal Maximum. Science 308 (5728), 1611–1615. https://doi.org/10.1126/science.1109004.

Zaïer, A., 1984. Etude stratigraphique et tectonique de la région de Sra Ouartane (Atlas tunisien central). Lithologie, pétrographie et minéralogie de la série phosphatée. These de Doct. 3ˆ< Eme> Cycle, Univ. de Tunis El Manar 158.

Zaïer, A., Beji-Sassi, A., Sassi, S., Moody, R., 1998. Basin evolution and deposition during the early Paleogene in Tunisia. Geol. Soc. Lond. Spec. Publ. 132 (1), 375–393.

Zhang, J., Amakawa, H., Nosaky, Y., 1994. The comparative behavior of Y and lanthanides in seawater on the North Pacific. Geophys. Res. Lett. 21, 2677–2680. https://doi.org/10.1029/94GL02404.

Zhang, S.H., Zhao, Y., Liu, Y., 2017. A precise zircon Th-Pb age of carbonatite sills from the world's largest Bayan Obo deposit: Implications for timing and genesis of REENb mineralization. Precambrian Res. 291, 202–219.

Zhao, X., Yang, K., Wei, Z., He, X., Chen, R., 2023. Study on the effect of multi-source solid waste on the performance of its backfill slurry. Heliyon 9 (5). https://doi.org/10.1016/j.heliyon.2023.e16251.

Zhao, X., Khelifi, F., Casale, M., Cavallo, A., Padoan, E., Yang, K., Dino, G.A., 2024. Critical raw materials supply: challenges and potentialities to exploit rare Earth elements from siliceous stones and extractive waste. Resources 13 (7), 97. https://doi.org/10.3390/resources13070097.